

# Learning Thermoelectric Transport from Crystal Structures via Multiscale Graph Neural Network

Yuxuan Zeng<sup>1</sup>, Wei Cao<sup>1,2,\*</sup>, Yijing Zuo<sup>2</sup>, Fang Lyu<sup>2</sup>, Wenhao Xie<sup>1</sup>,  
Tan Peng<sup>2</sup>, Yue Hou<sup>1</sup>, Ling Miao<sup>3</sup>, Ziyu Wang<sup>1,2,4,†</sup> and Jing Shi<sup>2</sup>

<sup>1</sup>*School of Integrated Circuits, Wuhan University, Wuhan 430072, PR China*

<sup>2</sup>*Key Laboratory of Artificial Micro- and Nano-Structures of Ministry of Education,  
School of Physics and Technology, Wuhan University, Wuhan 430072, PR China*

<sup>3</sup>*School of Optical and Electronic Information, Huazhong University of Science and Technology, Wuhan 430072, PR China*

<sup>4</sup>*School of Physics and Microelectronics, Key Laboratory of Materials Physics of Ministry of Education,  
Zhengzhou University, Zhengzhou 450001, PR China*

(Dated: December 9, 2025)

Graph neural networks (GNNs) are designed to extract latent patterns from graph-structured data, making them particularly well suited for crystal representation learning. Here, we propose a GNN model tailored for estimating electronic transport coefficients in inorganic thermoelectric crystals. The model encodes crystal structures and physicochemical properties in a multiscale manner, encompassing global, atomic, bond, and angular levels. It achieves state-of-the-art performance on benchmark datasets with remarkable extrapolative capability. By combining the proposed GNN with *ab initio* calculations, we successfully identify compounds exhibiting outstanding electronic transport properties and further perform interpretability analyses from both global and atomic perspectives, tracing the origins of their distinct transport behaviors. Interestingly, the decision process of the model naturally reveals underlying physical patterns, offering new insights into computer-assisted materials design.

## I. INTRODUCTION

Thermoelectric (TE) materials convert temperature gradients into electrical potential differences by driving carrier transport via the Seebeck effect [1]. This process involves no mechanical vibrations, produces no pollutant emissions, and is easy to integrate, making TE materials widely applicable in flexible and wearable electronic devices [2–4]. Evaluation of TE performance requires a comprehensive consideration of the Seebeck coefficient ( $S$ ), electrical conductivity ( $\sigma$ ), and thermal conductivity ( $\kappa$ ). These properties are collectively quantified by the dimensionless figure of merit,  $zT = \frac{S^2\sigma T}{\kappa}$ . The power factor, defined as  $PF = S^2\sigma$ , can also serve as an independent metric to assess the electrical transport performance of a material. The thermal transport in TE materials involves the combined contributions of both electronic and phononic carriers, i.e.,  $\kappa = \kappa_e + \kappa_{ph}$ . The corresponding electronic and phonon scattering mechanisms vary under different temperature and carrier conditions, making both  $\kappa_e$  and  $\kappa_{ph}$  crucial for the overall thermal conductivity performance [5]. Given the complexity of TE transport mechanisms and the nearly infinite combinations of elements and structures, traditional trial-and-error experimentation and *ab initio* computations, aimed at discovering potential outstanding TE materials, face significant challenges like high costs and long development cycles. Apparently, there is an increasing need for more efficient computational models and strategies to accelerate

the identification of promising TE materials.

To accelerate the high-throughput screening, artificial intelligence has emerged as a promising paradigm for exploring potential candidates [6, 7]. While machine learning techniques have been increasingly adopted to predict the properties of TE materials, accurately representing crystal structures remains a major challenge. Existing approaches either rely solely on chemical formulas [8–10] or employ empirical descriptors [11–13]. Features derived purely from chemical formulas have the advantage of being easy to construct, but they inherently overlook the influence of crystal topology on material properties. A representative example is diamond and graphite, which share the same chemical formula “C” but exhibit vastly different properties, e.g., diamond is an insulator, while graphite is a good conductor. Since lattice distortion serves as an important strategy in tuning TE transport [14, 15], structural representations are therefore indispensable. On the other hand, constructing empirical descriptors often requires resource-intensive *ab initio* calculations or experimental measurements.

To address above issues, an effective approach is to employ graph neural networks (GNNs) to model crystal structures for predicting their physicochemical properties. GNNs were first applied to molecules [16–18], owing to their discrete structures and accessible descriptors (e.g., SMILES [19]). In contrast, crystal modeling is more complicated due to structural periodicity and symmetry. CGCNN [20] tackled this challenge by applying graph convolutions to iteratively update atomic embeddings using neighbor and bond information. Building on this idea, a series of sophisticated derivatives have continuously improved predictive performance through clever architectural designs, consistently pushing the benchmark [21–24].

\* wei\_cao@whu.edu.cn

† zyuwang@whu.edu.cn

While such models achieve *ab initio*-level accuracy for general properties like formation energy ( $E_f$ ), band gap ( $E_g$ ), and bulk modulus, they often underperform in TE transport prediction [25], sometimes even lagging behind formula-based models [8]. This illustrates the *No Free Lunch* theorem [26], highlighting the necessity for task-specific designs. For instance, in predicting adsorption performance, simultaneously considering local structural attributes and global textural properties helps achieve state-of-the-art (SOTA) performance [27]. Likewise, the piezoelectric tensor depends on the choice of coordinate system and crystal symmetry, making it necessary to employ equivariant models that capture the relationship between crystal symmetry and the target tensor [28]. Therefore, learning TE transport also requires incorporating physics-guided design, rather than simply applying standard baseline models.

In this work, we propose a GNN-guided pipeline for high-throughput estimation of TE properties in inorganic crystalline materials. Beyond the commonly adopted atomic, bond, and angular features, we further incorporate global crystal-level descriptors to capture overarching physicochemical characteristics of the structure. Trained on a dataset [29] calculated by density functional theory (DFT), our model achieves SOTA accuracy in predicting TE transport properties. To enhance interpretability, we conduct sensitivity analysis to quantify the contribution of each input feature to the model output. Notably, this pipeline requires no domain-specific prior knowledge and offers a general and efficient tool to accelerate the discovery of promising TE materials.

## II. RESULTS

### A. Crystal graph representation and network architecture design

Graph, as a non-Euclidean data structure, is well-suited for representing complex topologies. An undirected graph  $\mathcal{G}$  consists of node vectors  $\mathbf{V}$  and edge vectors  $\mathbf{E}$ , i.e.,  $\mathcal{G} = (\mathbf{V}, \mathbf{E})$  [30]. In terms of fundamental properties alone, representing crystal information using  $(\mathbf{V}, \mathbf{E})$  is sufficient to achieve DFT-level accuracy. However, complex properties, including TE transport, are sensitive to structural variations such as bond angles and local geometric distortions. Therefore, introducing bond angles  $\Theta$  as an additional scale for crystal representation [22] is reasonable. In the specific context of TE transport, existing works indicate that global physicochemical properties of the crystal and their statistics (denoted as  $\mathbf{U}$ ) can achieve reliable accuracy and possess interpretable physical meaning [31, 32]. As noted in Sec. I, these descriptors are generated based on chemical formulas and lack structural representation. Our approach couples the formula-based descriptors  $\mathbf{U}$  with the structure-based  $(\mathbf{V}, \mathbf{E}, \Theta)$ , enabling multi-scale modeling of crystals, see Fig. 1.

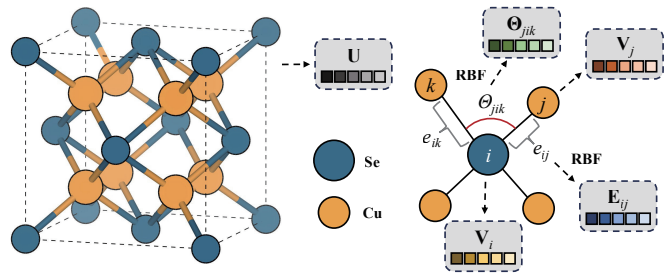


FIG. 1. Graph representation of crystal structures. Taking  $\text{CuSe}_2$  as an illustration, the crystal structure can be mathematically represented by a set of hierarchical vectorial descriptors at multiple scales, corresponding respectively to the global statistical properties, atomic sites, chemical bonds, and bond angles.

In GNNs, a distinctive operation known as “graph convolution” [33] is employed, which is similar to but also distinct from convolutions in convolutional neural networks (CNNs). In CNNs, convolutions aim to capture local patterns in images, such as edges, corners, and textures. Similarly, graph convolution in GNNs enables each node to aggregate information from its neighboring nodes, thereby refining its own embedding. In our case, we adopt a periodic  $k$ -nearest neighbors ( $k$ -NN) scheme, in which each atom in the primitive cell updates its embedding based on the  $k$  closest atoms and the corresponding edge information within the periodic lattice. In practice, we set  $k = 8$ ; smaller values may lead to information loss, whereas larger values significantly increase computational cost. It is important to note that  $k = 8$  does not limit the receptive field of an atom. Through multiple rounds of convolution, structural information from more distant atoms is also propagated to each node, albeit with diminishing influence, which aligns well with physical intuition [34].

As illustrated in Fig. 2, we term the proposed model the Thermoelectric Crystal Structure-Aware GNN (TECSA-GNN), which encodes atomic, bond, and angular information into a unified multigraph representation,

$$\mathcal{G} = (\mathbf{U}, \mathbf{V}_i, \mathbf{E}_{ij}, \Theta_{jik}), \quad (i, j, k) \in \mathcal{G}, \quad (1)$$

where  $\mathbf{V}_i$  denotes atom-wise features,  $\mathbf{E}_{ij}$  bond features,  $\Theta_{jik}$  angle features centered at atom  $i$ , and  $\mathbf{U}$  represents global crystal-level features (e.g., composition-weighted electronegativity, melting point, etc.). Both  $\mathbf{E}_{ij}$  and  $\Theta_{jik}$  are scalar inputs transformed into high-dimensional vectors using radial basis function (RBF) expansion [22, 35]. The detailed procedure of crystal graph representation is provided in Sec. IV B.

Initially, the embeddings  $\mathbf{V}$ ,  $\mathbf{E}$ , and  $\Theta$  possess disparate dimensionalities. To enable coherent subsequent graph convolution operations, they are projected onto a unified latent space via a multi-layer perceptron (MLP) module,

$$\mathbf{V}_i^{(0)}, \mathbf{E}_{ij}^{(0)}, \Theta_{jik}^{(0)} = \text{MLP}(\mathbf{V}_i, \mathbf{E}_{ij}, \Theta_{jik}). \quad (2)$$

After  $N$  graph convolution (GConv) layers, the model produces latent features  $\mathbf{H}^{(N)} = \{\mathbf{V}^{(N)}, \mathbf{E}^{(N)}, \Theta^{(0)}\}$

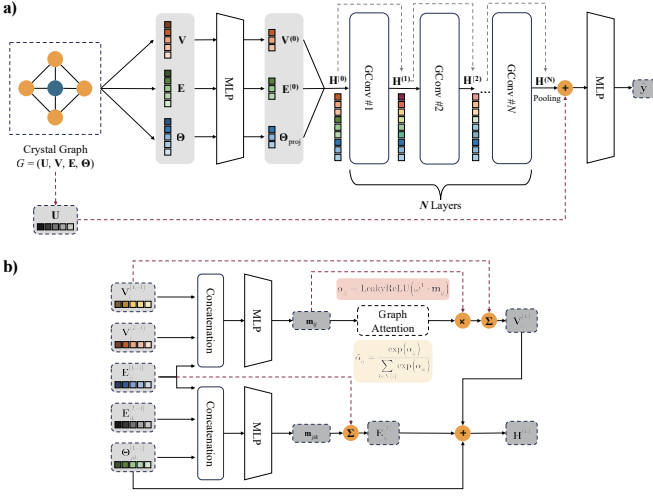


FIG. 2. The proposed GNN framework for crystal structure representation learning. (a) The overall architecture of the TECSA-GNN. Distinct colours are employed to indicate feature vectors at different scales. The superscript (0) designates the embedding representation subsequent to dimensional alignment by means of an MLP projection, whereas “ $N$ ” corresponds to the embedding yielded upon passage through the  $N$ -th graph convolutional module (GConv # $N$ ). (b) Detailed schematic of an individual graph convolutional module. In this representation, both “Concatenation” and “ $\oplus$ ” signify the concatenation of embeddings; “ $\sum$ ” denotes element-wise summation realised via residual connections; and “ $\otimes$ ” indicates element-wise multiplication.

(note that  $\Theta$  is fixed across layers). These representations are separately pooled and concatenated with  $\mathbf{U}$  for final prediction,

$$\hat{\mathbf{y}} = \text{MLP} \left( \text{Pool}(\mathbf{V}^{(N)}) \oplus \text{Pool}(\mathbf{E}^{(N)}) \oplus \mathbf{U} \right). \quad (3)$$

Through hierarchical message-passing, atoms and edges can incorporate information from their neighbors as well as embeddings from lower-level scales during convolution. This process proceeds in the order of  $\Theta \rightarrow \mathbf{E} \rightarrow \mathbf{V}$ . Each GConv layer updates atomic embeddings via graph attention [36],

$$\mathbf{m}_{i \leftarrow j} = \text{MLP} \left( \mathbf{v}_i^{(l-1)} \oplus \mathbf{v}_j^{(l-1)} \oplus \mathbf{e}_{ij}^{(l-1)} \right), \quad (4)$$

$$\tilde{\alpha}_{ij} = \text{softmax}_j \left( \text{LeakyReLU}(\omega^\top \mathbf{m}_{i \leftarrow j}) \right), \quad (5)$$

$$\mathbf{v}_i^{(l)} = \text{LN} \left( \mathbf{v}_i^{(l-1)} + \sum_{j \in \mathcal{N}(i)} \tilde{\alpha}_{ij} \mathbf{m}_{i \leftarrow j} \right), \quad (6)$$

and updates bond embeddings via a line graph convolution [22], incorporating angular information,

$$\mathbf{m}_{jik} = \text{MLP} \left( \mathbf{e}_{ij}^{(l-1)} \oplus \mathbf{e}_{ik}^{(l-1)} \oplus \Theta_{jik} \right), \quad (7)$$

$$\mathbf{e}_{ij}^{(l)} = \text{LN} \left( \mathbf{e}_{ij}^{(l-1)} + \frac{1}{|\mathcal{M}(k)|} \sum_{k \in \mathcal{M}(i,j)} \mathbf{m}_{jik} \right), \quad (8)$$

where  $\mathcal{M}(k)$  denotes the set of third atoms  $k$  that form angle triplets  $(j, i, k)$ . To ensure a good balance between computational efficiency and accuracy, each atom is connected to its 8 nearest-neighbors. Bonding and angular relations are extracted using the pymatgen toolkit [37].

## B. Quantitative evaluation, unsupervised learning and fine-tuning

In essence, TECSA-GNN may be regarded as a learnable function whose task is to map a crystal graph  $\mathcal{G}$  onto a quantitative descriptor of TE transport, denoted  $\mathcal{Y}$ , i.e.,  $(\mathcal{G}; \omega) \rightarrow \mathcal{Y}$ , where  $\mathcal{Y} = \{S, \sigma/\tau, \kappa_e/\tau\}$  represents the set of three canonical quantities employed to assess TE transport performance. The crystal graph  $\mathcal{G}$  is the abstract representation defined in Eq. (1), and  $\omega$  denotes the network parameters to be optimised during training. Concretely, the regression task is cast as the minimisation of a loss function, for which we adopt the mean squared error (MSE), i.e.,  $\mathcal{L} = \sum_{i=1}^{N_B} (y_i - \hat{y}_i)^2$ , where  $\hat{y}_i$  designates the model prediction of the target value, and  $N_B$  denotes the number of samples contained in a mini-batch, treated here as a hyperparameter.

In our case, the doping type and concentration of the material are concatenated with the global feature vector  $\mathbf{U}$  as part of the input representation, while model training is conducted under distinct temperature conditions. In addition, the band gap  $E_g$ , which constitutes one of the decisive parameters governing electronic transport properties, is directly provided by the dataset and likewise incorporated into  $\mathbf{U}$ . It must nevertheless be recognised that, for entirely unseen materials,  $E_g$  is typically unavailable. A practically effective remedy is to invoke SOTA pretrained models that infer  $E_g$  from the crystal structure *ab initio*, with the estimated value  $\hat{E}_g$  serving as a surrogate. Contemporary advances in AI-based prediction of  $E_g$  already permit accuracies commensurate with density functional theory; further details are given in [IV Supplementary Note 1](#).

In practice, we model  $\log(\sigma/\tau)$  and  $\log(\kappa_e/\tau)$  instead of  $\sigma/\tau$  and  $\kappa_e/\tau$  themselves to alleviate skewness arising from their wide-ranging distribution [38]. We employed 10-fold cross-validation to evaluate the predictive performance of the model. Fig. 3 illustrates the results for a fixed data split, where the training accuracy reflects the model’s learning capacity on the given dataset, while the validation accuracy quantifies its inference capability. Fig. 4 further presents how variations in data distribution, temperature, doping type, and doping concentration influence the model’s inference performance. Importantly, to prevent data leakage, all entries corresponding to the same material under different doping conditions were consistently assigned to the same subset. As anticipated, the prediction error for  $S$  is the smallest among the three targets, while the errors for  $\log(\sigma/\tau)$  and  $\log(\kappa_e/\tau)$  are comparable, largely reflecting the approximation inherent in  $\tau$ . Figs. 3(d)-(f) depict the training and validation

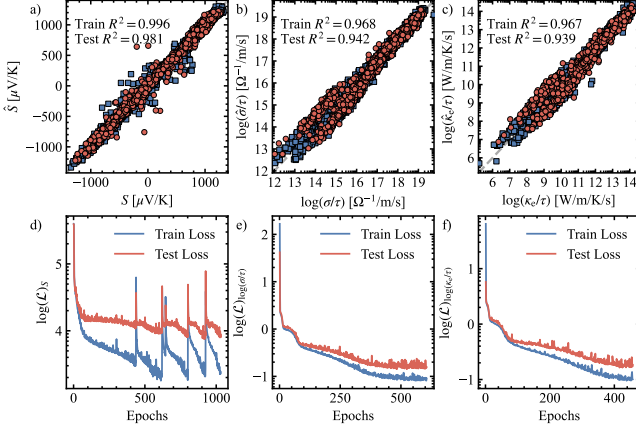


FIG. 3. Error evaluation for the TECSA-GNN model. (a)-(c) The parity plots for  $S$ ,  $\log(\sigma/\tau)$ , and  $\log(\kappa_e/\tau)$ , where red circles denote test samples and blue squares denote training samples. The  $x$ -axis represents the DFT-calculated values, and the  $y$ -axis shows the TECSA-GNN estimations. (d)-(f) The MSE loss curves for the training of  $S$ ,  $\log(\sigma/\tau)$ , and  $\log(\kappa_e/\tau)$ , with blue and red lines representing the training and test losses, respectively.

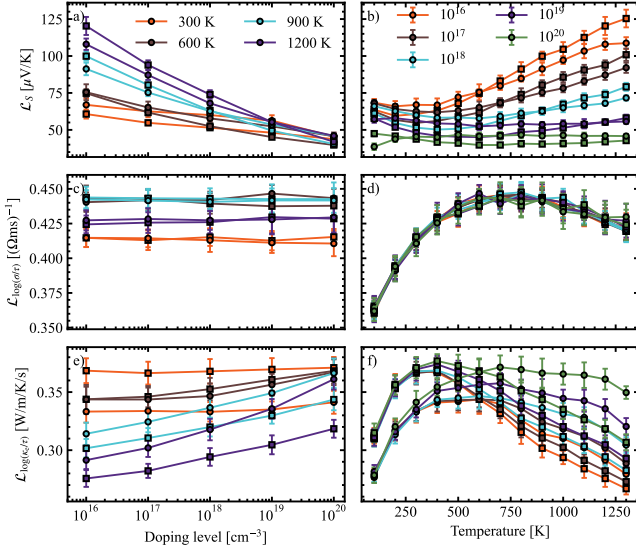


FIG. 4. 10-fold cross-validation performance of the TECSA-GNN. (a), (c), and (e) show the dependence of  $S$ ,  $\log(\sigma/\tau)$ , and  $\log(\kappa_e/\tau)$  on carrier concentration, with  $T = \{300, 600, 900, 1200\}$  K. (b), (d), and (f) depict the dependence of  $S$ ,  $\log(\sigma/\tau)$ , and  $\log(\kappa_e/\tau)$  on temperature, with  $n = \{10^{16}, 10^{17}, 10^{18}, 10^{19}, 10^{20}\}$   $\text{cm}^{-3}$ . Circular markers denote  $n$ -type samples, while square markers denote  $p$ -type. Error bars represent the mean and standard deviation of the MAE across the 10 folds.

loss curves;  $\mathcal{L}_{\text{Train}}$  and  $\mathcal{L}_{\text{Test}}$  for  $S$  are closely aligned, indicative of robust generalisation. Slight underfitting is observed for  $\log(\sigma/\tau)$  and  $\log(\kappa_e/\tau)$ , but overall accuracy remains acceptable. The principal advantage of TECSA-GNN lies in its unified architecture, which accommodates

the simultaneous learning of  $\{S, \sigma/\tau, \kappa_e/\tau\}$  without necessitating task-specific adjustments. For [GConv # $N$ ] in Fig. 2(a), we uniformly set  $N = 5$ , an empirically determined value balancing performance and efficiency. The only hyperparameter variation concerns the learning rate:  $\text{lr} = 0.01$  for  $S$ , and  $\text{lr} = 0.0001$  for  $\log(\sigma/\tau)$  and  $\log(\kappa_e/\tau)$ . Further details on hyperparameter settings are provided in IV Supplementary Note 2.

We provide a comprehensive benchmark to assess the accuracy of different models in estimating TE transport properties, as summarised in Tab. I. Among the models included for comparison, only CrabNet [39] characterises materials purely in terms of their chemical compositions, whereas all others are GNNs that exploit structural descriptors. In this benchmark, we follow the convention of Ref. [25] by setting the carrier concentration to  $n = 10^{19}$   $\text{cm}^{-3}$  and the temperatures to 600 K and 900 K, with separate evaluations performed for  $n$ -type and  $p$ -type doping. As compared in Tab. I, TECSA-GNN achieves SOTA performance in predicting TE properties, a result attributable to its comprehensive encoding of crystal structures together with the incorporation of physicochemical statistical features. It is worth emphasising that the *No Free Lunch* theorem applies equally to TECSA-GNN. We attempted to employ transfer learning [40] in order to train TECSA-GNN on the prediction of band gap  $E_g$  and formation energy  $E_f$ . Interestingly, although these targets are in principle learnable, the resulting accuracy was not particularly impressive when compared with peer models. This phenomenon may be ascribed to the tendency of overparameterised models to overfit: for relatively simple tasks, an excessive number of parameters risks capturing spurious noise within the data, thereby impairing generalisation [41]. By contrast, TE transport properties are intrinsically complex physical quantities, intimately linked to crystal structure, electronic structure, and physicochemical attributes. The choice of architectural complexity should therefore be made with due consideration of the physical context. For energy-related quantities such as  $E_g$  and  $E_f$ , ALIGNN [22] achieves SOTA performance, plausibly owing to its early incorporation of bond-angle information. Conversely, models relying solely on physicochemical statistical descriptors [42] perform markedly worse. In other words, for energy prediction tasks, structural descriptors alone may suffice. This reflects the spirit of *Occam's razor* [43]: adding more information or employing more complex architectures is not necessarily beneficial.

A practical approach of assessing whether the model has effectively captured structural information is to employ  $t$ -SNE [45] to project the samples into a low-dimensional map. For this purpose, we extract the activations from the final fully connected MLP layer preceding the output node  $\hat{y}$  (see Fig. 2) of the pre-trained  $S$  prediction model, and use them as sample representations. Here we chose the  $S$  pre-trained model since its prediction accuracy was the highest and thus most effective for learning structural representations, while the sign of  $S$  further indicates the

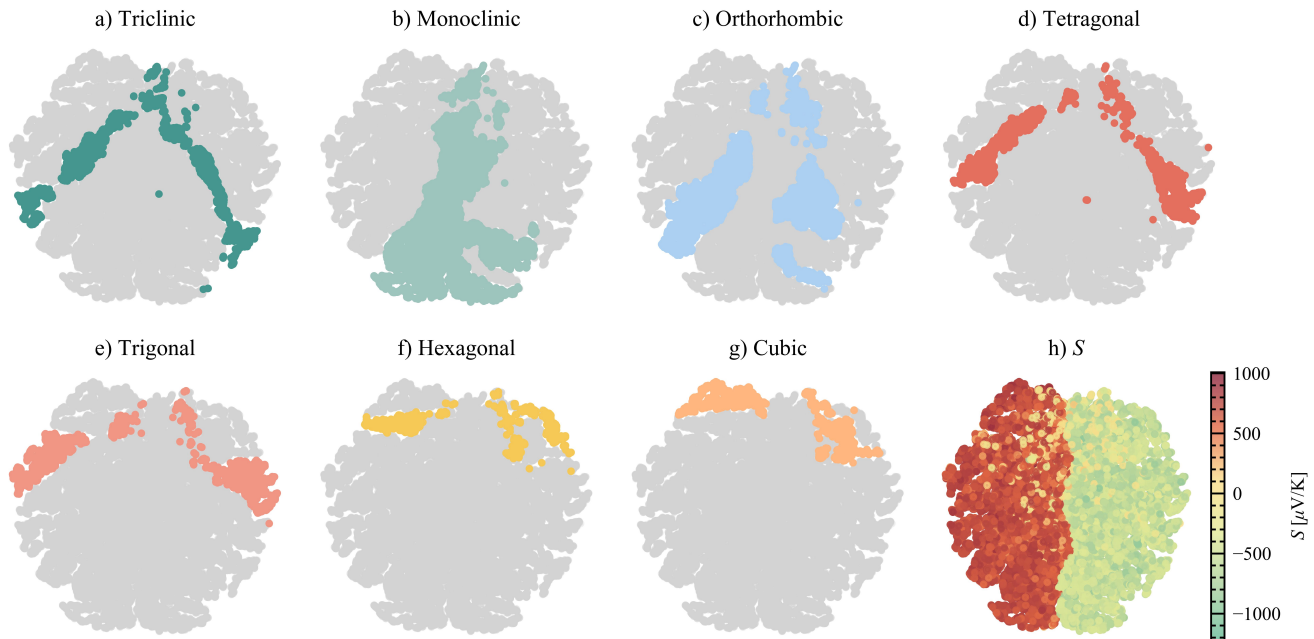


FIG. 5.  $t$ -SNE visualization of sample embeddings across different crystal systems. (a)-(g) Each colour denotes one of the seven crystal systems in the two-dimensional  $t$ -SNE plane, with grey points indicating samples from other systems. (h) Colour mapping of the Seebeck coefficient  $S$  illustrates both its magnitude and spatial distribution.

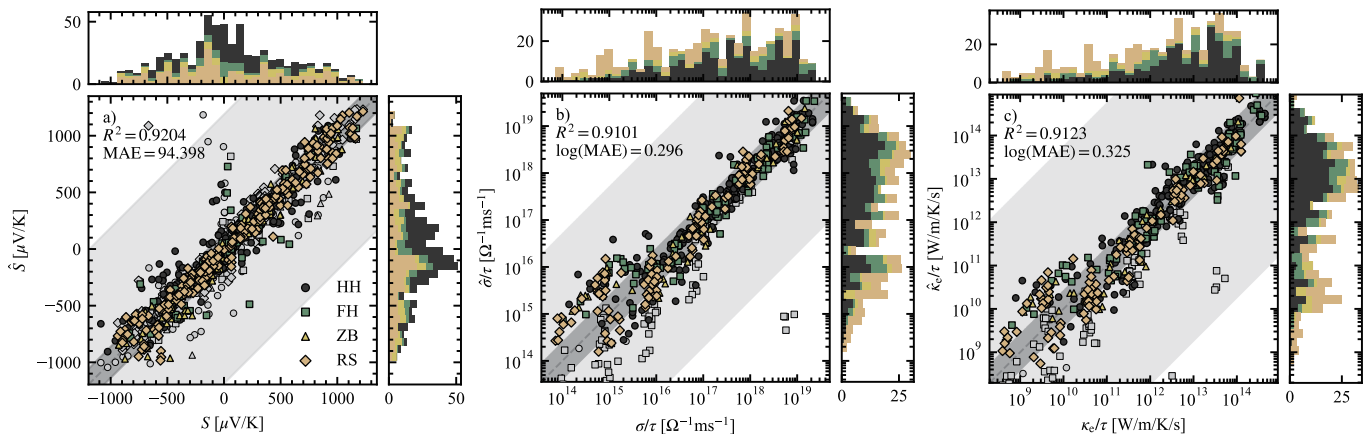


FIG. 6. Parity plots of TECSA-GNN after fine-tuning on special structures. (a)  $S$ , (b)  $\log(\sigma/\tau)$ , and (c)  $\log(\kappa_e/\tau)$ . Only test-set samples are shown. Circles, squares, triangles, and diamonds correspond to HH, FH, ZB, and RS structures. Grey markers denote predictions from the pretrained model, while coloured markers indicate predictions after fine-tuning. Light-grey bands represent one standard deviation of the prediction error of the pretrained model, with the corresponding range after fine-tuning shown in dark grey. Histograms along the top and right of each panel display the distributions of DFT reference values and model estimates, respectively.

doping type. A more detailed discussion of  $\log(\sigma/\tau)$  and  $\log(\kappa_e/\tau)$  is provided in [IV Supplementary Note 3](#), and the  $t$ -SNE visualization of the  $S$  model embeddings is shown in Fig. 5.

From the perspective of crystal structures, the distribution of materials from different crystal systems in the  $t$ -SNE space exhibits three salient features: first, samples of the same system form continuous and adjoining clusters; second, structurally similar systems, such as {Trigonal,

Hexagonal} or {Cubic, Tetragonal, Orthorhombic}, appear in close proximity; and third, the distributions of different doping types are arranged in an approximately symmetric manner. Continuity here refers to the clustering and adjacency of samples from the same crystal system, while proximity reflects the neighbourhood of structurally related systems. These phenomena indicate that the embeddings learned by TECSA-GNN contain sufficiently rich structural information, for only under

TABLE I. Benchmark of test set results in terms of MAE for TE transport properties and basic material properties. Bold values indicate SOTA performance. For the carrier concentration, we adopt the standard setting of  $n = 10^{19} \text{ cm}^{-3}$ .

Property	Unit	Temp.	Type	CrabNet [39]	CGCNN [20]	GeoCGNN [44]	ALIGNN [22]	CraLiGNN [25]	TECSA-GNN
$S$			$n$	89.024	109.11	97.72	84.267	74.645	<b>60.686</b>
$S$	$\mu\text{V}/\text{K}$	600 K	$p$	86.812	113.32	104.97	80.925	79.79	<b>54.333</b>
$S$			$n$	86.756	92.528	106.53	81.815	74.685	<b>66.079</b>
$S$	$\mu\text{V}/\text{K}$	900 K	$p$	96.165	102.26	111.37	88.203	81.209	<b>66.408</b>
$\log(\sigma/\tau)$			$n$	0.563	0.586	0.526	0.493	0.454	<b>0.265</b>
$\log(\sigma/\tau)$	$\log(\Omega\text{ms})^{-1}$	600 K	$p$	0.615	0.568	0.559	0.497	0.46	<b>0.293</b>
$\log(\sigma/\tau)$			$n$	0.608	0.540	0.518	0.471	0.429	<b>0.261</b>
$\log(\sigma/\tau)$	$\log(\Omega\text{ms})^{-1}$	900 K	$p$	0.601	0.547	0.556	0.502	0.438	<b>0.286</b>
$\log(\kappa_e/\tau)$			$n$	0.634	0.598	0.563	0.546	0.476	<b>0.352</b>
$\log(\kappa_e/\tau)$	$\log(\text{W}/\text{m}/\text{K}/\text{s})$	600 K	$p$	0.662	0.612	0.609	0.559	0.504	<b>0.365</b>
$\log(\kappa_e/\tau)$			$n$	0.586	0.564	0.555	0.493	0.449	<b>0.350</b>
$\log(\kappa_e/\tau)$	$\log(\text{W}/\text{m}/\text{K}/\text{s})$	900 K	$p$	0.603	0.538	0.582	0.513	0.449	<b>0.319</b>
$E_g$	eV	-	-	0.271	0.400	0.289	<b>0.224</b>	-	0.397
$E_f$	eV/atom	-	-	0.081	0.040	0.030	<b>0.022</b>	-	0.054

this condition can samples with identical or similar structures appear close in the low-dimensional space [45, 46]. Symmetry, on the other hand, is manifested in the near left-right reflection of different systems. As shown in Fig. 5(h), a possible explanation is that the horizontal axis encodes the qualitative separation of doping type, with  $n$ -type materials on the left and  $p$ -type on the right; intriguingly, some samples located in the upper region exhibit  $S$  values opposite to their nominal doping type, a behaviour that may be associated with bipolar conduction phenomena [47, 48].

We masked a set of special crystal structures in the dataset and evaluated the generalisation ability of TECSA-GNN on unseen configurations by fine-tuning the pre-trained model. In practice, a total of 133 special structures (covering Full-Heusler (FH), Half-Heusler (HH), rocksalt (RS), and zinc blende (ZB) phases) were considered. Unlike in pretraining, these samples were evenly divided into training and testing subsets. Moreover, it was unnecessary to retrain all model parameters: the MLPs used for dimensional alignment and all GConv layers were kept frozen, and only the terminal regression head was fine-tuned. This strategy improves computational efficiency and preserves the stability of local feature extraction, while allowing the model to adapt specifically to these special structures without discarding prior knowledge.

Fig. 6 compares the performance of pretrained and fine-tuned models at 300 K for four representative structures. Fine-tuning offers two principal advantages: first, it selectively improves predictions for these special structures, most notably by reducing outlier errors; second, it avoids the considerable computational cost of training from scratch, requiring only  $\sim 50$  epochs in our case to achieve substantial accuracy gains. It should be noted, however, that the  $R^2$  metric is inherently correlated with sample size [49]; consequently, the values reported in Fig. 6 are lower than those in Fig. 3. Across datasets of unequal size, MAE is a more dependable metric.

### C. Discovering potential thermoelectric materials

Leveraging the pretrained TECSA-GNN model, we screened unlabeled data to identify promising candidates with potentially high PF values. The Materials Project [50] provides a vast repository of crystal structures along with DFT-computed band gaps. We applied the following criteria to filter candidate materials: (1) contains Sb, Te or Se, (2)  $0 < E_g < 1.5$  [eV], (3) nonmagnetic, (4) free of transition metals, and (5) fewer than 20 atomic sites in the unit cell ( $n_{\text{sites}} < 20$ ). Criteria (1) and (2) are empirical in nature: elements such as Sb, Te, and Se are frequently encountered in TE materials, while constraining the band gap  $E_g$  ensures that candidates fall within the semiconducting regime. Meanwhile, criteria (3), (4) and (5) are motivated primarily by the need to simplify subsequent DFT calculations. After excluding materials already present in our training dataset, we conducted DFT validations on three promising candidates at 300 K: [mp-1209957] NaTlSe<sub>2</sub>, [mp-9897] Te<sub>3</sub>As<sub>2</sub> and [mp-1207082] LiMgSb.

Among them, NaTlSe<sub>2</sub> was previously reported by Ref. [8], albeit with analysis limited to its chemical formula, whereas our GNN-based approach enables structural evaluation at the crystal level. Recent studies suggest that a PF exceeding  $6.8 \times 10^{-4}$  [W/m/K<sup>2</sup>] (as in  $p$ -type SnSe) [51] or  $8 \times 10^{-4}$  [W/m/K<sup>2</sup>] (as in  $n$ -type Sc<sub>0.015</sub>Mg<sub>3.185</sub>Sb<sub>1.5</sub>Bi<sub>0.47</sub>Te<sub>0.03</sub>) [52] can be considered qualitatively high at 300 K. In Fig. 7, the  $\kappa_e$  of the candidates remains below 1 [W/m/K] across the considered doping range. From a TE perspective, however, this does not necessarily imply a low overall thermal conductivity, since  $\kappa_{\text{ph}}$  is typically the dominant contribution to heat transport [53]. Nevertheless, when  $\kappa_{\text{ph}}$  itself is sufficiently low and becomes comparable in magnitude to  $\kappa_e$ , the electronic contribution can no longer be neglected in evaluating the total thermal transport performance [54].

Overall, TECSA-GNN shows good agreement with DFT calculations, particularly in the estimation of  $S$ . The pre-

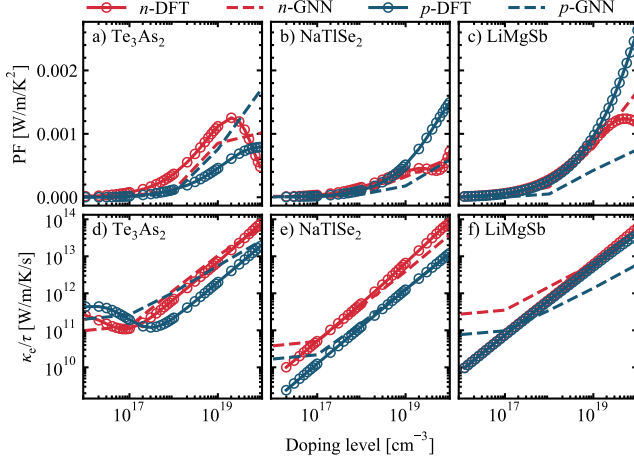


FIG. 7. Comparison between TE transport properties predicted by the TECSA-GNN model and those obtained from DFT calculations. (a)-(c) display the PF values of  $\text{Te}_3\text{As}_2$ ,  $\text{NaTlSe}_2$ , and  $\text{LiMgSb}$ , computed as  $S^2\sigma/\tau \times 10^{-14}$  rather than directly learned by TECSA-GNN. (d)-(f) show the corresponding  $\kappa_e/\tau$ . Red and blue denote  $n$ -type and  $p$ -type carriers, respectively; solid lines represent DFT-calculated trajectories, while dashed lines indicate TECSA-GNN predictions. Circular symbols mark the DFT-sampled data points, and the trajectories are obtained through smooth fitting.

dictions of  $\sigma/\tau$  and  $\kappa_e/\tau$  are somewhat less accurate, yet as discussed in Sec. II B, the dataset’s approximation of the relaxation time  $\tau$  inevitably introduces some uncertainty. Despite these errors, the efficiency of a pretrained AI model compared with *ab initio* calculations makes it highly practical for high-throughput screening of new materials, enabling the rapid identification of promising candidates across vast, unexplored regions of compositional and structural space. In addition to  $\text{NaTlSe}_2$ ,  $\text{Te}_3\text{As}_2$ , and  $\text{LiMgSb}$ , we also provide predictions for other unlabeled samples, as detailed in IV Supplementary Note 6.

#### D. Tracing thermoelectric behaviour from DFT insights

Taking the candidates in Sec. II C as examples, we performed DFT calculations of their band structures and electron localization functions (ELF) to trace the origin of their TE performance.

In Fig. 8, the band structures of  $\text{Te}_3\text{As}_2$ ,  $\text{LiMgSb}$ , and  $\text{NaTlSe}_2$  exhibit distinct features. For  $\text{Te}_3\text{As}_2$ , both the conduction band minimum (CBM) and the valence band maximum (VBM) are located near  $E_{\text{Fermi}}$ , indicating a small  $E_g$  and a nearly metallic character. The pronounced band dispersion around  $E_{\text{Fermi}}$  further implies a small  $m^*$ . According to Mott’s formula for the Seebeck coefficient [55],  $S$  is closely related to the energy-dependent

gradients of the density of states and scattering strength,

$$S = \frac{\pi^2 k_B^2 T}{3e} \left. \frac{d \ln \sigma(E)}{dE} \right|_{E=E_{\text{Fermi}}}, \quad (9)$$

where  $\sigma(E) = e^2 N(E) v^2(E) \tau(E)$  represents the energy-dependent conductivity, with  $\tau$  fixed at  $10^{-14}$  s in our case. In Fig. 8(a), the steeply dispersive bands of  $\text{Te}_3\text{As}_2$  indicate slowly varying  $v(E)$  and a relatively flat  $N(E)$ , resulting in a small conductivity gradient near  $E_{\text{Fermi}}$ , i.e.,  $\frac{d \ln \sigma(E)}{dE} \propto \frac{d(\ln N(E) v^2(E) \tau(E))}{dE}$ , and consequently a low  $S$  [56]. In fact, the excellent PF of  $\text{Te}_3\text{As}_2$  arises from its exceptionally high  $\sigma$ , consistent with its nearly metallic nature. As illustrated in Fig. 7(e),  $\text{Te}_3\text{As}_2$  exhibits a markedly larger  $\kappa_e/\tau$  than  $\text{LiMgSb}$  and  $\text{NaTlSe}_2$ , which further corroborates this feature.

According to Fig. 8(b) and (c),  $\text{LiMgSb}$  and  $\text{NaTlSe}_2$  exhibit several common features in their band structures. The VBM lies close to  $E_{\text{Fermi}}$ , indicating hole-dominated conduction under intrinsic or lightly acceptor-doped conditions, consistent with the general trend that  $p$ -type TE materials usually achieve higher PF values [57]. The cations contribute negligibly to the dominant states near the band edges; for instance, the projected density of states (PDOS) of Li in  $\text{LiMgSb}$  and Na in  $\text{NaTlSe}_2$  is nearly zero, suggesting that these ions mainly act as electrostatic charge balancers rather than active contributors to transport. Unlike conventional thermoelectrics where cations participate in transport, Li/Na here play a unique charge-balancing role. The Na layers stabilize the Tl-Se framework and influence the geometry of Tl-Se bonds, thereby tuning the  $d$ - $p$  hybridization [58] strength and the position of the VBM. This behavior aligns with previous findings that alkali cations in chalcogenide thermoelectrics act as electrostatic modulators rather than electronic contributors [59]. The valence bands of  $\text{NaTlSe}_2$  are relatively flat, leading to large carrier effective masses and low mobility, and hence low  $\sigma$ , but the steep variation of the DOS near  $E_{\text{Fermi}}$  yields a large  $\frac{d \ln \sigma(E)}{dE}$  and thus a high  $S$ . The flat-band nature and localization of states, however, suppress carrier mobility, limiting  $\sigma$  and leading to a low electronic thermal conductivity  $\kappa_e$ . Overall,  $\text{NaTlSe}_2$  represents a system characterized by high  $S$ , low  $\sigma$ , and low  $\kappa_e$ . Similarly,  $\text{LiMgSb}$  exhibits negligible Li orbital contributions near the valence and conduction bands, with Li ion acting mainly as an electrostatic stabilizer. The valence bands are dominated by Sb- $d$  orbitals, while the conduction bands are primarily Mg- $d$  in character, indicating that hole transport is governed by the Sb sublattice and electron transport occurs mainly within the Mg-Sb framework [60]. The strongly dispersive valence bands in  $\text{LiMgSb}$  indicate small  $m^*$ , which, according to the relation  $\mu \propto 1/m^*$ , lead to high carrier mobility and thus high  $\sigma$ . Conversely, flat valence bands (i.e., low dispersion) would correspond to large  $m^*$  and reduced  $\mu$  [56]. Meanwhile, the small DOS gradient results in a lower  $S$ , and the delocalized nature of the bands contributes to an elevated  $\kappa_e$ . Overall,  $\text{LiMgSb}$  exhibits a balanced

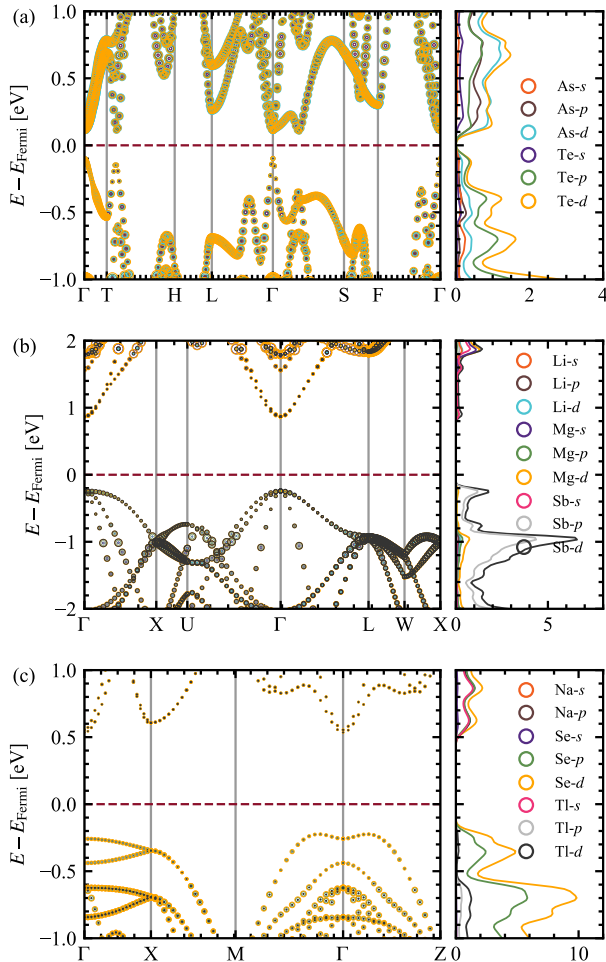


FIG. 8. Projected band structure and PDOS. (a)  $\text{Te}_3\text{As}_2$ , (b)  $\text{LiMgSb}$ , (c)  $\text{NaTlSe}_2$ . In the left panel, each scatter represents the atomic-orbital projection weight at a given  $k$  point and energy, with color denoting the atomic species and marker area proportional to the PDOS value of the corresponding atom and orbital, normalized by the maximum PDOS of that atom. Vertical lines indicate the high-symmetry  $k$ -points, and the dashed horizontal line marks the Fermi level. The right panel shows the PDOS curves of each atom in the same colors as in the band plot, where solid, dashed, and dotted lines correspond to the  $s$ -,  $p$ -, and  $d$ -orbital contributions, respectively.

combination of transport properties, with moderate  $S$ , high  $\sigma$ , and intermediate  $\kappa_e$ .

Apart from the electronic band structure, the electron localization function (ELF) [61] offers further theoretical insight into the distinct TE behaviours of the candidate materials. The ELF directly reflects the extent of electron localization or delocalization, a key factor governing carrier mobility and thus the electronic transport coefficients. Its values range from  $[0, 1]$ : when  $\text{ELF} \approx 1$ , it indicates strong electron localization, as in covalent bonds or lone-pair regions; when  $\text{ELF} \approx 0.5$ , it corresponds to a delocalized, nearly homogeneous electron gas typical of metallic conduction; lower ELF values generally denote

regions of sparse electron density, such as interionic voids.

We calculated the ELF distributions of  $\text{Te}_3\text{As}_2$ ,  $\text{LiMgSb}$ , and  $\text{NaTlSe}_2$ , as shown in Fig. 9. The atoms in  $\text{Te}_3\text{As}_2$  exhibit a layered arrangement, and the ELF map in Fig. 9(d) reveals a distinctive layered covalent framework. As illustrated in Fig. 9(a), a high degree of electron localisation occurs between Te and As atoms within the layers, forming strongly directional covalent bonds. This is consistent with the PDOS in Fig. 8(a), where both As and Te contribute markedly near the CBM and VBM. In contrast, Te-Te and As-As interactions show clear delocalisation, and almost no electron density is observed between the layers. The ELF characteristics of  $\text{Te}_3\text{As}_2$  closely resemble those of  $\text{SnSe}$ , both displaying interlayer voids and enhanced metallicity [62]. Overall, this interplay of intralayer localisation and interlayer delocalisation gives rise to pronounced band dispersion (particularly along the  $\Gamma$ -L direction), leading to a reduced  $m^*$ , higher carrier mobility, and consequently an increased  $\sigma$  [63].

A distinctive feature of the 3D ELF of  $\text{LiMgSb}$  (see Fig. 9(e)) is the strong localization around Sb atoms, while Mg exhibits a delocalized character, with island-like localized regions distributed between Mg-Mg atoms. Li, on the other hand, is almost fully ionized. In general, when electrons are strongly confined to specific atoms or bonds in real space (such as in lone pairs or strong covalent bonds), their wavefunctions spread broadly in momentum space, resulting in weak band dispersion. This leads to a large effective mass  $m^*$  and consequently reduced mobility [64]. In the case of  $\text{LiMgSb}$ , the Sb- $p$  electrons are localized but moderately hybridized with Mg, which manifests in the band structure as weakly dispersive, yet not completely flat, bands. This feature accounts for the relatively high  $S$  and the lower  $\sigma$  and  $\kappa_e$ , respectively. Unlike  $\text{LiMgSb}$ , where island-like ELF regions appear between Mg-Mg atoms, Fig. 9(f) shows that the ELF of  $\text{NaTlSe}_2$  is fully localized around Se atoms. In other words,  $\text{NaTlSe}_2$  exhibits stronger localization and greater anion character than  $\text{LiMgSb}$ . This results in flat valence-band tops, as seen along the  $\Gamma$ -Z-P direction in Fig. 8(c), which correlate with strong ELF localization ( $> 0.9$ ) around Se atoms. Such localization induces low band dispersion and hence large  $m^*$ , enhancing  $S$  via  $S \propto m^*$ . Consequently,  $\text{NaTlSe}_2$  exhibits the highest  $S$  but the lowest  $\sigma$  and  $\kappa_e$  among the three candidates. Taken together, these results reveal the intrinsic antagonism between  $S$  and  $\sigma$  in TE materials. Therefore, among the three compounds considered,  $\text{LiMgSb}$ , which maintains the most balanced combination of  $S$  and  $\sigma$ , achieves the highest PF, as shown in Fig. 7.

### E. Input sensitivity quantification and graph interpretation

Interpretability [65] is a central theme across ‘‘AI for Science’’ [66]. In contrast to traditional AI applications such as computer vision, which are often dominated by

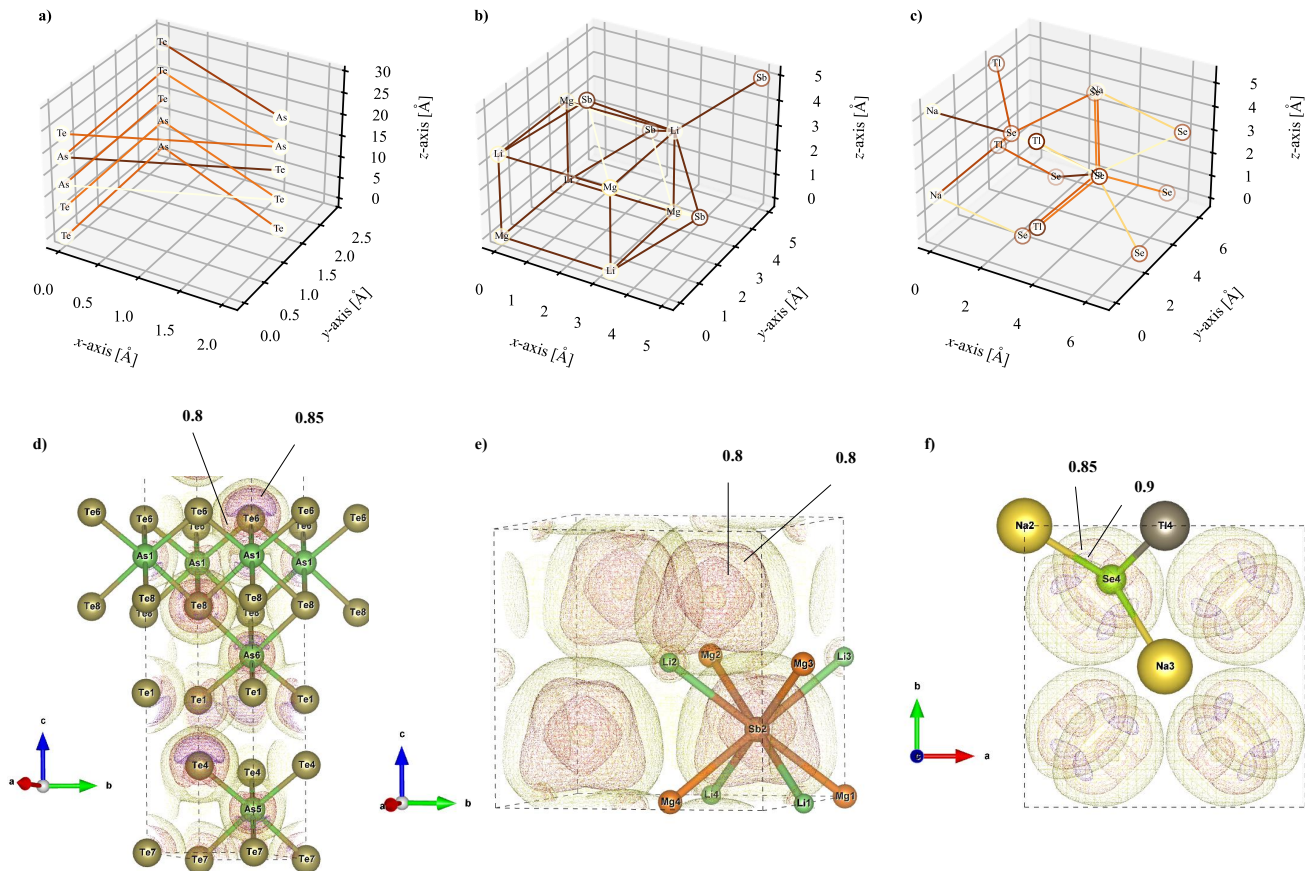


FIG. 9. Atomic importance and ELF spatial visualization. In the unit cells of (a)  $\text{Te}_3\text{As}_2$ , (b)  $\text{LiMgSb}$ , and (c)  $\text{NaTiSe}_2$ , the front-back position of each atom is indicated by transparency, while the atomic importance is encoded through the colour gradient of the edge highlights, with darker brown signifying greater contribution to the TECSA-GNN decision. The diagrams also show the mean ELF values between pairs of atoms; only connections with an average ELF  $> 0.4$  are displayed, as values below this threshold suggest weak or negligible bonding. Darker lines correspond to ELF values approaching 1, whereas lighter lines approach 0.4. Subplots (d)–(f) present the ELF spatial distributions for  $\text{Te}_3\text{As}_2$ ,  $\text{LiMgSb}$ , and  $\text{NaTiSe}_2$ , respectively, with isosurfaces defined at selected ELF levels.

black-box models and the sole pursuit of SOTA performance, “AI for Science” places greater emphasis on enabling AI models to reflect or even uncover underlying theoretical patterns. In practice, the complex topology and message-passing mechanisms make GNNs particularly challenging to interpret. Interpretation methods can be categorized into four groups [67]: gradient-, perturbation-, decomposition-, and surrogate-based methods. In brief, gradient-based methods [68] compute the gradient of the output with respect to input features, where larger magnitudes indicate greater importance; perturbation-based methods [69] mask nodes, edges, or their combinations to observe changes in the output; decomposition-based methods [70] disentangle the prediction process to trace contributions of inputs across layers; and surrogate-based methods [71] approximate the GNN with a simpler but more interpretable model.

In this work, we adopt different strategies to interpret the TECSA-GNN across multiple feature scales. Specifically, we use the GNNEXPLAINER [72] to assess the

contribution of atomic embeddings  $\mathbf{V}$  at the atomistic scale; apply perturbation-based methods to evaluate the importance of bond features  $\mathbf{E}$ ; and, for global crystal features  $\mathbf{U}$ , employ a lightweight MLP surrogate as a practical solution. Considering that among the TE quantities learned by TECSA-GNN only  $S$  corresponds to an actual physical value, while both  $\sigma/\tau$  and  $\kappa_e/\tau$  involve the relaxation-time approximation and thus contain inherent uncertainties, all subsequent interpretability analyses are conducted with  $S$  as the research object.

Let us begin with a simple case. To investigate how the global features  $\mathbf{U}$  influence the prediction of  $S$ , we constructed a  $128 \times 128 \times 128$  MLP as a surrogate model, where crystal structure features were completely excluded. We first attempted to assess feature importance using SHapley Additive Explanations (SHAP) method [73]. However, apart from the band gap  $E_g$ , which consistently exhibited the highest SHAP value, the intervention effects of other top-ranked features on the predicted  $S$  were rather ambiguous (see IV Supplementary Note 4). It is

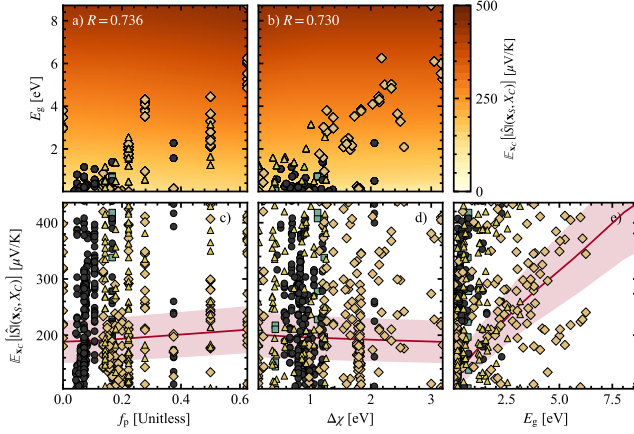


FIG. 10. Partial dependence plots of the key global features for the Seebeck coefficient  $S$ . When the varying feature set  $\mathbf{x}_S$  is fixed as (a)  $\{E_g, f_p\}$ , (b)  $\{E_g, \Delta\chi\}$ , (c)  $\{f_p\}$ , (d)  $\{\Delta\chi\}$ , and (e)  $\{E_g\}$ , the estimated values of  $\mathbb{E}_{\mathbf{X}_C} [|\hat{S}|(\mathbf{x}_S, \mathbf{X}_C)]$  are shown. In (a) and (b),  $\mathbb{E}_{\mathbf{X}_C} [|\hat{S}|(\mathbf{x}_S, \mathbf{X}_C)]$  is a bivariate function obtained by uniform sampling within the ranges of each feature. In (c)-(e),  $\mathbb{E}_{\mathbf{X}_C} [|\hat{S}|(\mathbf{x}_S, \mathbf{X}_C)]$  degenerates to a univariate function controlled solely by the variable on the  $x$ -axis. The red curve denotes the target dependence on the current variable, the pink band represents the 20% uncertainty interval, and the marker shapes are consistent with Fig. 6, corresponding to HH, FH, ZB, and RS structures, with black circles representing other conventional structures.

worth noting, nevertheless, that both  $f_p$  and  $\Delta\chi$  showed strong linear correlations with  $E_g$ . Here,  $f_p$  denotes the fraction of elements with  $p$ -orbital valence electrons, while  $\Delta\chi$  is defined as the difference between the maximum and minimum electronegativity among the constituent elements. Therefore, we retained  $\{E_g, f_p, \Delta\chi\}$  for further discussion of their respective physical impacts on  $S$ . Fig. 10 illustrates the partial dependence [74] of  $|\hat{S}|$  on  $\{E_g, f_p, \Delta\chi\}$ , where a subset of variables  $\mathbf{x}_S$  is selected and the remaining features  $\mathbf{X}_C$  are fixed at their mean values to remove irrelevant variation, such that the estimation of  $|S|$  is written as  $\mathbb{E}_{\mathbf{X}_C} [|\hat{S}|(\mathbf{x}_S, \mathbf{X}_C)]$ . Here we focus on  $|S|$  rather than  $S$  itself in order to eliminate the sign change induced by the doping type, since in evaluating TE performance only the absolute magnitude of  $S$ , i.e.,  $|S|$ , is of interest.

In Fig. 10, the most evident trend is that  $E_g$  shows a obvious positive correlation with  $|S|$ . The transport integral for  $S$  [75, 76] is defined as

$$S = -\frac{k_B}{e} \int \left( \frac{E - E_{\text{Fermi}}}{k_B T} \frac{\sigma(E)}{\sigma} \right) dE, \quad (10)$$

where  $k_B$  is the Boltzmann constant,  $e$  is the elementary charge,  $E$  is the energy of the electronic state,  $E_{\text{Fermi}}$  is the Fermi level,  $T$  is the absolute temperature, and the term  $\sigma(E)/\sigma$  represents the normalized transport distri-

bution function, i.e., the relative contribution of carriers at energy  $E$  to the total electrical conductivity. From the perspective of Eq. 10,  $S$  may be simply interpreted as the weighted energy shift of carriers relative to  $E_{\text{Fermi}}$ . When  $E_g$  is small, both valence- and conduction-band states near  $E_{\text{Fermi}}$  are thermally accessible, so that  $\sigma(E)$  is distributed on both sides of  $E_{\text{Fermi}}$  and the integral term  $(E - E_{\text{Fermi}})$  in Eq. 10 cancels out, thereby reducing the average energy shift and lowering  $|S|$ . This corresponds to the so-called bipolar conduction phenomenon [77]. A larger  $E_g$  benefits  $S$  by mitigating thermal excitation, suppressing the minority-carrier population, and thus weakening bipolar conduction [78].

As illustrated in Fig. 10(c) and (d), the effects of  $f_p$  and  $\Delta\chi$  on  $|\hat{S}|$  are less direct than that of  $E_g$ , and such features typically influence model predictions only through interactions with others [79]. Nevertheless, Fig. 10(a) and (b) reveal a rough yet interesting trend: larger  $f_p$  and  $\Delta\chi$  tend to be associated with higher  $E_g$ , thereby indirectly enhancing  $|\hat{S}|$ . Electronegativity  $\chi$  is a measure of an element's ability to attract electrons within a compound, and its contribution to  $E_g$  can be divided into covalent and ionic parts: the former is governed by the average electronegativity  $\bar{\chi}$  of the compound, while the latter is determined by  $\Delta\chi$  [80]. Specifically, D. Adams [81] proposed the following definition of  $E_g$ ,

$$E_g^2 = E_h^2 + C^2, \quad (11)$$

where  $E_h^2$  denotes the covalent contribution to the  $E_g$ , determined by  $\bar{\chi}$ , and  $C$  is the charge-transfer energy, directly correlated with  $\Delta\chi$ .

By contrast, the role of  $f_p$  in determining  $E_g$  is less clear. Ref. [82] speculated that increasing  $f_p$  enhances the interaction at the band edges and thereby enlarges  $E_g$ , though no conclusive evidence was provided. Inspired by Ref. [80], we conjecture that  $f_p$  influences  $E_g$  indirectly via its effect on  $\chi$ . In Fig. 10(b), within the approximate range  $\Delta\chi < 1.4$  [eV],  $E_g$  and  $\Delta\chi$  are in fact roughly anticorrelated; compounds in this regime tend to be covalent [83] (strictly speaking  $\Delta\chi < 1.7$  [eV]), whereas larger  $\Delta\chi$  favours ionic bonding. In covalent compounds,  $p$ -orbital electrons dominate the bonding and antibonding states, and the band gap arises from the energy difference between the valence-band maximum (typically  $p$ -like) and the conduction-band minimum (of  $s/p$  or  $s/d$  hybrid character). When  $f_p$  is high, the valence-band maximum is pushed upward by  $p$  states, often reducing  $E_g$  [84]. In ionic compounds, however, a large  $\Delta\chi$  enhances the contribution of anion  $p$  states to the valence band, which raises  $f_p$  and leads to a larger gap [85]. Thus,  $\Delta\chi$  may be the more direct driver of band-gap enlargement, while an increase in  $f_p$  may merely reflect the concomitant effect of increasing  $\Delta\chi$ .

The sensitivity analysis with respect to  $\mathbf{U}$  applies to the entire materials space, whereas for specific candidates, e.g.,  $\text{Te}_3\text{As}_2$ ,  $\text{LiMgSb}$ , and  $\text{NaTiSe}_2$ , one may quantify the influence of individual atoms on the model's decision

at the atomic scale, denoted by  $\mathbf{V}$ . This can be achieved through single-node explanations provided by GNNEXPLAINER [72]. The detailed implementation of GNNEXPLAINER will be presented in Sec. IV C. Briefly, it evaluates the importance of a node by comparing the change in the model’s output before and after masking that node. Using this approach, we performed atomic-node importance analyses for  $\text{Te}_3\text{As}_2$ ,  $\text{LiMgSb}$ , and  $\text{NaTlSe}_2$ , and found that atomic importance is, to some extent, correlated with the degree of electronic localisation and the contribution of each element to the PDOS. In Fig. 9(a)-(c), the normalized importance values assigned by GNNEXPLAINER to each atom in the prediction of  $S$  are mapped by color.

Fig. 9(a) shows that all atoms in  $\text{Te}_3\text{As}_2$  exhibit zero importance, indicating that the atomic features  $\mathbf{V}$  of  $\text{Te}_3\text{As}_2$  play an almost negligible role in the model’s estimation of  $S$  for this compound. From a physical standpoint, this phenomenon may stem from the delocalisation of electronic states, leading the decisive variables to become global in nature. Although the electrons around Te and As atoms are highly localised (high ELF), orbital hybridisation occurs between layers, resulting in wavefunction delocalisation along the interlayer direction in band space. According to Eq. 10, the Seebeck coefficient  $S$  depends on the asymmetry of the bands near the Fermi energy  $E_{\text{Fermi}}$  and on the global transport function,

$$\sigma(E) \sim \sum_{\mathbf{k},n} v_{n\mathbf{k}}^2 \tau_{n\mathbf{k}} \delta(E - E_{n\mathbf{k}}), \quad (12)$$

where  $n$  denotes the band index,  $\mathbf{k}$  is the wavevector in the Brillouin zone,  $v_{n\mathbf{k}}$  is the electron group velocity,  $\tau_{n\mathbf{k}}$  is the relaxation time, and  $E_{n\mathbf{k}}$  is the band energy. This expression shows that the energy-dependent conductivity  $\sigma(E)$  represents a weighted accumulation of transport contributions from all bands and  $\mathbf{k}$  points, governed jointly by the squared electron velocity, scattering lifetime, and density of states. In many semimetals or narrow-gap systems where the Fermi surface is dominated by highly delocalised Bloch states,  $\sigma(E)$  is determined by the overall band structure and the average velocity or relaxation time. Local atomic perturbations are often “diluted” by such averaging effects, resulting in only minor changes to the overall shape of  $\sigma(E)$  [86]. Nevertheless, when local perturbations introduce resonant or trap states or significantly modify the local transition matrix elements, thereby changing the density of states or carrier lifetimes near the  $E_{\text{Fermi}}$ , single-site variations can still exert a pronounced influence on  $\sigma(E)$  and on derived physical quantities such as  $S$  [86].

In the semiconductors  $\text{MgLiSb}$  and  $\text{NaTlSe}_2$ , the relative importance of individual atoms appears to be closely linked to their specific roles in the electronic band structure. Qualitatively, as shown in Fig. 9(b), the Sb atoms in  $\text{MgLiSb}$  exhibit higher importance than Li and Mg; whereas in Fig. 9(c), Se shows slightly greater importance than Tl, with Na consistently being the least important. Examining the band structures in Fig. 8(b) and (c), one

finds that these importance values qualitatively reflect the dominant orbital contributions of different elements: in  $\text{LiMgSb}$ , the VBM is almost entirely governed by Sb, while Li and Mg show negligible features in their PDOS near either the CBM or the VBM. In contrast, in  $\text{NaTlSe}_2$ , Se and Tl jointly determine the shape of the CBM, whereas the VBM is almost exclusively controlled by Se.

### III. DISCUSSION

The proposed multiscale GNN model, TECSA-GNN, accurately captures the complex and nonlinear relationships between crystal structures and TE transport properties. By integrating global compositional features with atomic, bond, and angular representations within a unified message-passing framework, the model achieves outstanding predictive performance on a large DFT-computed dataset. Among the three key TE descriptors, the Seebeck coefficient  $S$  shows the most reliable prediction, which arises from the model’s ability to effectively learn intrinsic connections between electronic structure and band topology.

Beyond improved accuracy, TECSA-GNN reveals physically consistent trends that align with conventional transport theory. The model identifies a positive correlation between  $|S|$  and the band gap  $E_g$ , reflecting the suppression of bipolar conduction in wide-gap materials, consistent with the Mott relation. Interpretability analyses further indicate that for systems dominated by localized states such as  $\text{NaTlSe}_2$  and  $\text{LiMgSb}$ , the network assigns greater importance to atoms associated with lone-pair orbitals or covalent distortions, in agreement with the PDOS and ELF results. In contrast, for delocalized or nearly metallic systems such as  $\text{Te}_3\text{As}_2$ , the importance distribution becomes more uniform, suggesting that the model’s decisions rely on overall band dispersion rather than localized chemical motifs. These consistent patterns demonstrate that the learned representations encode not only numerical correlations but also the underlying physical mechanisms governing TE transport.

The multiscale architecture of TECSA-GNN plays a decisive role in both performance and interpretability. Hierarchical message propagation from angular to bond to atomic levels allows the model to aggregate short-range geometrical distortions and long-range chemical contexts, which are essential for transport properties determined by orbital hybridization and band connectivity. The inclusion of composition-level descriptors further enhances the transferability of the model, enabling efficient fine-tuning across different chemical families. This multilevel coupling effectively bridges the gap between empirical descriptors and first-principles calculations, establishing a generalizable paradigm for high-throughput screening.

However, some intrinsic limitations of our work should be emphasised. The assumption of a constant relaxation time  $\tau = 10^{-14}$  s, while common in transport databases, cannot reflect variations among materials caused by de-

fects, temperature, or phonon scattering, which limits the absolute prediction of  $\sigma$  and  $\kappa_e$ . Furthermore, reducing anisotropic tensors to scalar averages may overlook directional effects in layered or low-symmetry systems. Although multiple interpretability approaches such as GNNEXPLAINER, perturbation analysis, and surrogate MLP models highlight meaningful features, the distinction between statistical relevance and true causality should be treated cautiously since nonlinear feature entanglement may obscure direct physical attribution.

Future improvements can proceed along four directions. First, incorporating relaxation-time models based on phonon spectra or empirical scattering approximations would enhance the physical realism of the predictions. Second, applying uncertainty quantification through ensemble or Bayesian techniques [87] could provide confidence intervals for large-scale material screening. Third, employing equivariant GNNs [88] that preserve tensorial symmetry would allow direct prediction of anisotropic transport tensors. Lastly, coupling these developments with active learning and iterative DFT validation would establish an efficient closed-loop framework for material discovery [89].

In summary, TECSA-GNN successfully establishes a physically consistent mapping between atomic geometry and TE transport by encoding multiscale structural and electronic information. Its strong predictive power and interpretability provide a solid foundation for integrating machine learning with first-principles calculations, offering a promising pathway toward accelerated discovery of high-performance TE materials and deeper understanding of structure–property relationships.

## IV. METHODS

### A. Creating the dataset

The training dataset employed in this work originates from the DFT calculations of Ref. [29]. The original dataset comprises a total of 47,737 materials, each evaluated under both  $n$ - and  $p$ -type doping conditions, 5 carrier concentrations ranging from  $10^{16}$  to  $10^{20}$  cm $^{-3}$ , and 13 temperature points spanning 100 K to 1300 K. For each setting, the TE properties  $S$ ,  $\sigma$ , and  $\kappa_e$  are reported. After removing samples with missing information, duplicates, elemental single-component systems, and those for which feature construction failed, a total of 16,637 valid entries were retained. It is worth noting that, owing to crystalline anisotropy, the TE properties are provided in the form of  $3 \times 3$  matrices,

$$\mathbf{y} = \begin{pmatrix} y_{xx} & y_{xy} & y_{xz} \\ y_{yx} & y_{yy} & y_{yz} \\ y_{zx} & y_{zy} & y_{zz} \end{pmatrix}. \quad (13)$$

For the sake of simplification, we consider the normalized trace of  $\mathbf{y}$ , defined as  $y = \frac{1}{3}\text{Tr}[\mathbf{y}]$ , which yields a

scalar quantity that is subsequently adopted as the learning target of the model.

An important subtlety is that the conductivity values reported in the dataset do not, in fact, correspond to the absolute conductivity but rather to the conductivity normalised by the relaxation time, namely the intrinsic conductivity  $\sigma/\tau$ , where  $\tau = 10^{-14}$  s. This quantity is determined solely by the electronic structure of the material, e.g., the carrier concentration  $n$  and the effective mass  $m^*$  [90]. The relaxation time  $\tau$ , meanwhile, encapsulates the underlying scattering processes in the crystal, governed by a multitude of factors including temperature, defects, and impurities [91, 92], and its explicit computation remains notoriously difficult. The adoption of  $\sigma/\tau$  is therefore a widely employed simplification: whilst intrinsic conductivity is not strictly identical to the measurable conductivity, it nonetheless serves as a meaningful proxy for assessing the propensity of a material to behave as either a good conductor or an insulator [93].

### B. Transforming the crystal structures into graph representations

In Eq. 1, each crystal is represented in terms of its topological and physicochemical characteristics at four hierarchical levels: global, atomic, bond, and angular. The global feature vector  $\mathbf{U}$  is constructed using the Magpie descriptors [94], which provide elemental physicochemical properties such as melting point and electronegativity based on the constituent elements, and compute statistical quantities such as the mean, variance, and extrema, weighted by the stoichiometric ratios. Similarly, the atomic feature vector  $\mathbf{V}$  is derived following the same scheme; however, for individual atoms, statistical measures are redundant. Therefore,  $\mathbf{V}$  records the intrinsic physicochemical properties of each element, whereas  $\mathbf{U}$  captures the statistical aggregates. In practice, the normalized atomic coordinates are concatenated into the atomic feature vector,  $\mathbf{V}_i = \mathbf{r}_i^{\text{norm}} \oplus f_{\text{elem}}(a_i)$ .

For each atomic pair  $(a_i, a_j)$ , the scalar distance is computed from their coordinates  $\{\mathbf{r}_i, \mathbf{r}_j\}$  as  $d_{ij} = \|\mathbf{r}_i - \mathbf{r}_j\|$ . In addition, the normalized bond direction vector is defined as  $\hat{\mathbf{u}}_{ij} = \frac{\mathbf{r}_j - \mathbf{r}_i}{\|\mathbf{r}_j - \mathbf{r}_i\|}$ , which is concatenated with the RBF embedding of bond length to form the final bond feature.

For each atomic triplet  $(a_j, a_i, a_k)$ , we define the directional vectors  $\{\mathbf{u} = \mathbf{r}_j - \mathbf{r}_i, \mathbf{v} = \mathbf{r}_k - \mathbf{r}_i\}$ , and the bond angle is given by  $\theta_{jik} = \arccos\left(\frac{\mathbf{u} \cdot \mathbf{v}}{\|\mathbf{u}\|\|\mathbf{v}\|}\right)$ . Both  $\{d_{ij}, \theta_{jik}\}$  are further transformed into vectors by the RBF expansion as

$$\begin{cases} \mathbf{V}_{ij} = \exp\left(-\frac{(d_{ij} - \mu_d)^2}{\sigma_d^2}\right), \\ \Theta_{jik} = \exp\left(-\frac{(\theta_{jik} - \mu_\theta)^2}{\sigma_\theta^2}\right). \end{cases} \quad (14)$$

In our implementation, the RBF expansion for bond lengths covers the range  $[0, 8]$  Å, with center parameters

$\mu_k = \text{linspace}(0, 8, 8)$ , a center spacing of  $\Delta_d = 8/7 \approx 1.14 \text{ \AA}$ , and a width parameter of  $\sigma_d = 1.5\Delta_d \approx 1.71 \text{ \AA}$ . For bond angles, the RBF expansion spans  $[0, \pi]$ , with centers  $\nu_m = \text{linspace}(0, \pi, 8)$ , spacing  $\Delta_\theta = \pi/7 \approx 0.45$ , and width  $\sigma_\theta = 1.5\Delta_\theta \approx 0.67$ . This Gaussian-type expansion constructs a set of smooth and differentiable basis functions in continuous geometric space, effectively enabling the neural network to analytically capture structural variations within local geometric neighborhoods (receptive fields). It finely resolves local differences in bond lengths and angles, while the continuous kernel representation enhances smoothness and transferability in learning non-linear relationships [95, 96].

---

**Algorithm 1: Representing Crystal Graph**

---

**Input:** Crystal structure  $\mathcal{C}$  (.cif), global descriptors  $\mathbf{U}$ , band gap  $E_g$ , doping type  $t \in \{0, 1\}$  ( $\{0\}$  for  $n$ -type), doping level  $n \in \{10^{16}, 10^{17}, \dots, 10^{20}\} \text{ cm}^{-3}$ .

**Output:** Multiscale graph  $\mathcal{G} = (\mathbf{U}, \mathbf{V}, \mathbf{E}, \Theta)$

- 1 **Step 1: Atom Features**
- 2 Extract normalized coordinates and element-wise vectors:

$$\mathbf{V}_i = \mathbf{r}_i^{\text{norm}} \oplus f_{\text{elem}}(a_i)$$

- 3 **Step 2: Bond Features**
- 4 Construct  $k$ -NN graph with periodic boundary:

$$d_{ij} = \text{dist}(a_i, a_j), \quad j \in \mathcal{N}_k(i)$$

Apply RBF expansion and concatenate direction vector:

$$\mathbf{E}_{ij} = \hat{\mathbf{u}}_{ij} \oplus \phi_{\text{RBF}}(d_{ij})$$

- 5 **Step 3: Angular Features**
- 6 Build line graph:

$$\theta_{jik} = \angle(a_j, a_i, a_k)$$

Apply RBF expansion:

$$\Theta_{jik} \leftarrow \phi_{\text{RBF}}(\theta_{jik})$$

- 7 **Step 4: Global Features**
- 8 Concatenate physicochemical descriptors:

$$\mathbf{U} = f_{\text{global}}(\mathcal{C}) \oplus n \oplus t \oplus E_g(\mathcal{C})$$

- 9 **Step 5: Assemble Graph**

$$\mathcal{G} = (\mathbf{U}, \mathbf{V}_i, \mathbf{E}_{ij}, \Theta_{jik}), \quad (i, j, k) \in \mathcal{C}$$

11 **return**  $\mathcal{G}$

---

Alg. 1 illustrates how TECSA-GNN constructs graph representations. This process compresses the complex crystal structure into a machine-readable embedding vector.

### C. Evaluating the atom/node importance via GNNEXPLAINER

For a pretrained GNN model  $f_\theta(\mathcal{G}) \rightarrow y$ , GNNEXPLAINER [72] aims to identify a minimal subset of atomic nodes whose presence is sufficient to preserve the original prediction, i.e.,  $f_\theta(\mathcal{G}_s) \approx f_\theta(\mathcal{G})$ . Since direct optimisation over discrete node selections is NP-hard, GNNEXPLAINER introduces a continuous node-masking mechanism [97]. Each atom  $a_i$  is associated with a learnable mask parameter  $M_i \in [0, 1]$  that controls its contribution to message passing. The masked graph is represented as

$$\begin{cases} \mathbf{H}' = \mathbf{H} \odot \sigma(\mathbf{M}_v), \\ \hat{y}_t = f_\theta(\mathcal{G}, \mathbf{H}'), \end{cases} \quad (15)$$

where  $\mathbf{H} \in \mathbb{R}^{N \times d}$  is the node feature matrix with  $N$  atoms and  $d$ -dimensional descriptors,  $\mathbf{M}_v \in \mathbb{R}^N$  is a learnable continuous node mask,  $\sigma(\cdot)$  is the sigmoid function constraining each mask value to  $[0, 1]$ , and  $\hat{y}_t$  is the predicted output for the masked graph. To enforce predictive fidelity and encourage sparsity and smoothness, the following loss is defined:

$$\begin{cases} \mathcal{L}_{\text{pred}} &= [f_\theta(\mathcal{G}, \mathbf{H}') - f_\theta(\mathcal{G}, \mathbf{H})]^2, \\ \mathcal{L}_{\text{reg}} &= \alpha \|\mathbf{M}_v\|_1 + \beta \left[ -\sigma(\mathbf{M}_v) \log(\sigma(\mathbf{M}_v)) \right. \\ &\quad \left. - (1 - \sigma(\mathbf{M}_v)) \log(1 - \sigma(\mathbf{M}_v)) \right], \\ \min_{\mathbf{M}_v} \mathcal{L} &= \mathcal{L}_{\text{pred}} + \mathcal{L}_{\text{reg}}, \end{cases} \quad (16)$$

where  $\alpha$  and  $\beta$  control the sparsity and smoothness of the mask, respectively. The mask parameters are updated via gradient descent:

$$\mathbf{M}_v \leftarrow \mathbf{M}_v - \eta \frac{\partial \mathcal{L}}{\partial \mathbf{M}_v}. \quad (17)$$

After convergence, the learned mask becomes sparse, isolating the critical atoms that dominate the model's prediction. Nodes with higher mask values indicate the regions of chemical or structural significance, forming the local explanatory subgraph  $\mathcal{G}_s$ .

### D. DFT calculations

DFT calculations in this work were performed using the Vienna *Ab-initio* Simulation Package (VASP) [98]. The projector augmented wave (PAW) method was employed to describe the electron-ion interactions [98, 99]. The exchange-correlation functional was treated within the generalized gradient approximation (GGA) as parameterized by Perdew-Burke-Ernzerhof (PBE) [100]. A plane-wave cutoff energy of 500 eV was used, and the electronic self-consistent iteration was converged to within  $10^{-8}$  eV. Structural optimizations were carried out using  $k$ -point meshes generated with VASPKIT [101], with a  $k$ -spacing of  $0.03 \text{ \AA}^{-1}$ . TE transport coefficients were evaluated by solving the linearized Boltzmann transport equation as implemented in the BoltzTraP2 code [102].

## ACKNOWLEDGMENTS

We would like to acknowledge the National Key Research and Development Program of China (Grant No. 2023YFB4603800), the financial support from the project of the National Natural Science Foundation of China (Grants No. 12404062, No. 12474093, No. 12302220, No. 12374091), Translational Medicine and Interdisciplinary Research Joint Fund of Zhongnan Hospital of Wuhan University (Grant No. ZNJC202235), and the Fundamental Research Funds for the Central Universities (Grant No. 2042023kf0109). The numerical calculations in this work have been done on the supercomputing system in the Supercomputing Center of Wuhan University.

## Data Availability

The data that support the findings of this article are openly available [103].

## Code Availability

The codes that support the findings of this article are openly available [103].

## Competing Interests

The authors declare no competing interests.

- 
- [1] J. He and T. M. Tritt, *Science* **357**, eaak9997 (2017).
- [2] X. Sun, Y. Hou, Z. Zhu, B. Zhu, Q. Ding, W. Zhou, S. Yan, Z. Xia, Y. Liu, Y. Hou, *et al.*, *Nat. Commun.* **16**, 1 (2025).
- [3] W. Yang, Y. Zhong, D. Ao, D. Yang, M. Wei, F. Li, Y. Chen, G. Liang, J. Luo, and Z. Zheng, *Appl. Phys. Lett.* **126**, 123902 (2025).
- [4] D. Kraemer, Q. Jie, K. McEnaney, F. Cao, W. Liu, L. A. Weinstein, J. Loomis, Z. Ren, and G. Chen, *Nat. Energy* **1**, 1 (2016).
- [5] T. Y. Kim, C.-H. Park, and N. Marzari, *Nano Lett.* **16**, 2439 (2016).
- [6] J. Moi, D. Spallarossa, S. Bonetti, R. Burioni, and G. Caldarelli, *Phys. Rev. E* **112**, 011001 (2025).
- [7] J. Leeman, Y. Liu, J. Stiles, S. B. Lee, P. Bhatt, L. M. Schoop, and R. G. Palgrave, *PRX Energy* **3**, 011002 (2024).
- [8] L. M. Antunes, K. T. Butler, and R. Grau-Crespo, *Mach. Learn.: Sci. Technol.* **4**, 015037 (2023).
- [9] Y. Xu, L. Jiang, and X. Qi, *Comput. Mater. Sci.* **197**, 110625 (2021).
- [10] M. Al-Fahdi, K. Yuan, Y. Yao, R. Rurali, and M. Hu, *Appl. Phys. Rev.* **11**, 021402 (2024).
- [11] J. Yan, P. Gorai, B. Ortiz, S. Miller, S. A. Barnett, T. Mason, V. Stevanović, and E. S. Toberer, *Energy Environ. Sci.* **8**, 983 (2015).
- [12] M. Y. Toriyama, A. N. Carranco, G. J. Snyder, and P. Gorai, *Mater. Horiz.* **10**, 4256 (2023).
- [13] X. Huang, S. Ma, C. Zhao, H. Wang, and S. Ju, *npj Comput. Mater.* **9**, 191 (2023).
- [14] W. Cao, J. Shi, R. Xiong, L. Miao, Z. Wang, and Z. Liu, *Phys. Rev. B* **107**, 235201 (2023).
- [15] F. Lyu, W. Cao, H.-P. Liang, T. Peng, Y. Hou, X. Zhu, L. Miao, Z. Wang, R. Xiong, and J. Shi, *J. Mater. Chem. A* **12**, 18452 (2024).
- [16] F. Scarselli, M. Gori, A. C. Tsoi, M. Hagenbuchner, and G. Monfardini, *IEEE Trans. Neural Netw.* **20**, 61 (2008).
- [17] Y. Wang, J. Wang, Z. Cao, and A. Barati Farimani, *Nat. Mach. Intell.* **4**, 279 (2022).
- [18] C. W. Coley, R. Barzilay, W. H. Green, T. S. Jaakkola, and K. F. Jensen, *J. Chem. Inf. Model.* **57**, 1757 (2017).
- [19] A. M. Veselinovic, J. B. Veselinovic, J. V. Zivkovic, and G. M. Nikolic, *Curr. Top. Med. Chem.* **15**, 1768 (2015).
- [20] T. Xie and J. C. Grossman, *Phys. Rev. Lett.* **120**, 145301 (2018).
- [21] H. Choubisa, P. Todorović, J. M. Pina, D. H. Parmar, Z. Li, O. Voznyy, I. Tamblin, and E. H. Sargent, *npj Comput. Mater.* **9**, 117 (2023).
- [22] K. Choudhary and B. DeCost, *npj Comput. Mater.* **7**, 185 (2021).
- [23] M. Karamad, R. Magar, Y. Shi, S. Siahrostami, I. D. Gates, and A. Barati Farimani, *Phys. Rev. Mater.* **4**, 093801 (2020).
- [24] C. W. Park and C. Wolverton, *Phys. Rev. Mater.* **4**, 063801 (2020).
- [25] Z. Wang, R. Hu, X. Luo, and J. Ma, *J. Appl. Phys.* **136**, 155103 (2024).
- [26] D. Gómez and A. Rojas, *Neural Comput.* **28**, 216 (2016).
- [27] E. Lin, Y. Zhong, G. Chen, and S. Deng, *npj Comput. Mater.* **11**, 225 (2025).
- [28] L. Dong, X. Zhang, Z. Yang, L. Shen, and Y. Lu, *npj Comput. Mater.* **11**, 63 (2025).
- [29] F. Ricci, W. Chen, U. Aydemir, G. J. Snyder, G.-M. Rignanese, A. Jain, and G. Hautier, *Sci. Data* **4**, 1 (2017).
- [30] Z. Wu, S. Pan, F. Chen, G. Long, C. Zhang, and P. S. Yu, *IEEE Trans. Neural Netw. Learn. Syst.* **32**, 4 (2020).
- [31] K. Vipin and P. Padhan, *J. Mater. Chem. C* **12**, 7415 (2024).
- [32] H. Choubisa, M. A. Haque, T. Zhu, L. Zeng, M. Vafaie, D. Baran, and E. H. Sargent, *Adv. Mater.* **35**, 2302575 (2023).
- [33] M. Niepert, M. Ahmed, and K. Kutzkov, in *Int. Conf. Mach. Learn.*, Proc. Mach. Learn. Res., Vol. 48 (PMLR, New York, New York, USA, 2016) pp. 2014–2023.
- [34] W. G. Zeier, A. Zevalkink, Z. M. Gibbs, G. Hautier, M. G. Kanatzidis, and G. J. Snyder, *Angew. Chem. Int. Ed.* **55**, 6826 (2016).
- [35] F. M. A. Acosta, *Signal Proc.* **45**, 37 (1995).
- [36] P. Veličković, G. Cucurull, A. Casanova, A. Romero, P. Liò, and Y. Bengio, in *Int. Conf. Learn. Represent.* (2018).
- [37] S. P. Ong, W. D. Richards, A. Jain, G. Hautier, M. Kocher, S. Cholia, D. Gunter, V. L. Chevrier, K. A. Persson, and G. Ceder, *Comput. Mater. Sci.* **68**, 314 (2013).

- [38] J. P. Higgins, I. R. White, and J. Anzures-Cabrera, *Stat. Med.* **27**, 6072 (2008).
- [39] A. Y.-T. Wang, S. K. Kauwe, R. J. Murdock, and T. D. Sparks, *npj Comput. Mater.* **7**, 77 (2021).
- [40] S. J. Pan and Q. Yang, *IEEE Trans. Knowl. Data Eng.* **22**, 1345 (2010).
- [41] C. Mingard, H. Rees, G. Valle-Pérez, and A. A. Louis, *Nat. Commun.* **16**, 220 (2025).
- [42] J. Li, Z. Chen, J. Wu, J. Lin, P. He, R. Zhu, C. Peng, H. Zhang, W. Li, X. Fang, and H. Shen, *Mater. Today Commun.* **35**, 106299 (2023).
- [43] R. Dhahri, A. Immer, B. Charpentier, S. Günnemann, and V. Fortuin, in *Adv. Neural Inform. Process. Syst.*, Vol. 37 (Curran Associates, Inc., 2024) pp. 24959–24989.
- [44] J. Cheng, C. Zhang, and L. Dong, *Commun. Mater.* **2**, 92 (2021).
- [45] L. v. d. Maaten and G. Hinton, *J. Mach. Learn. Res.* **9**, 2579 (2008).
- [46] H. Zhang, P. Wang, X. Gao, Y. Qi, and H. Gao, *Inf. Visualization* **20**, 20 (2021).
- [47] S. Foster and N. Neophytou, *Comput. Mater. Sci.* **164**, 91 (2019).
- [48] P. Graziosi, Z. Li, and N. Neophytou, *Appl. Phys. Lett.* **120**, 072102 (2022).
- [49] M. D. McKay, M. A. Fitzgerald, and R. J. Beckman (Los Alamos National Lab., NM (US), 1999).
- [50] A. Jain, S. P. Ong, G. Hautier, W. Chen, W. D. Richards, S. Dacek, S. Cholia, D. Gunter, D. Skinner, G. Ceder, *et al.*, *APL Mater.* **1**, 10.1063/1.4812323 (2013).
- [51] B. Su, Z. Han, Y. Jiang, H.-L. Zhuang, J. Yu, J. Pei, H. Hu, J.-W. Li, Y.-X. He, B.-P. Zhang, *et al.*, *Adv. Funct. Mater.* **33**, 2301971 (2023).
- [52] L. Yu, X.-L. Shi, Y. Mao, M. Li, W.-D. Liu, Z. Ji, S. Wei, Z. Zhang, W. Song, S. Zheng, and Z.-G. Chen, *Chem. Eng. J.* **482**, 149051 (2024).
- [53] Q. Xu, J. Zhou, T.-H. Liu, and G. Chen, *Appl. Phys. Lett.* **115**, 023903 (2019).
- [54] C. Wan, Y. Wang, N. Wang, W. Norimatsu, M. Kusunoki, and K. Koumoto, *Sci. Technol. Adv. Mater.* **11**, 044306 (2010).
- [55] J. M. Buhmann and M. Sigrist, *Phys. Rev. B* **88**, 115128 (2013).
- [56] J. Park, Y. Xia, V. Ozoliņš, and A. Jain, *npj Comput. Mater.* **7**, 43 (2021).
- [57] J. Yang, G. Zhang, G. Yang, C. Wang, and Y. X. Wang, *J. Alloys Compd.* **644**, 615 (2015).
- [58] Z.-H. Liu, P. Richard, N. Xu, G. Xu, Y. Li, X.-C. Fang, L.-L. Jia, G.-F. Chen, D.-M. Wang, J.-B. He, T. Qian, J.-P. Hu, H. Ding, and S.-C. Wang, *Phys. Rev. Lett.* **109**, 037003 (2012).
- [59] D. Wang, Y. Chao, K. Guo, Z. Wang, M. Yang, J. Zhu, X. Cui, and Q. Xu, *Adv. Funct. Mater.* **34**, 2405642 (2024).
- [60] T. Gnanapoongothai, R. Murugan, and B. Palanivel, *Ionics* **21**, 1351 (2015).
- [61] A. Savin, R. Nesper, S. Wengert, and T. F. Fässler, *Angew. Chem. Int. Ed.* **36**, 1808 (1997).
- [62] S. Siddique, G. Abbas, M. M. Yaqoob, J. Zhao, R. Chen, J. A. Larsson, Y. Cao, Y. Chen, Z. Zheng, D. Zhang, and F. Li, *Adv. Sci.* **12**, 2411594 (2025).
- [63] B. A. Williamson, J. Buckeridge, J. Brown, S. Ansbro, R. G. Palgrave, and D. O. Scanlon, *Chem. Mater.* **29**, 2402 (2017).
- [64] W. Zhao, P. Wei, Q. Zhang, H. Peng, W. Zhu, D. Tang, J. Yu, H. Zhou, Z. Liu, and X. Mu, *Nat. Commun.* **6**, 6197 (2015).
- [65] X. Jiang, H. Fu, Y. Bai, L. Jiang, H. Zhang, W. Wang, P. Yun, J. He, D. Xue, T. Lookman, *et al.*, *Adv. Funct. Mater.* , 2507734 (2025).
- [66] Q. Miao and F.-Y. Wang, in *Artificial Intelligence for Science (AI4S) Frontiers and Perspectives Based on Parallel Intelligence* (Springer, 2024) pp. 105–113.
- [67] H. Yuan, H. Yu, S. Gui, and S. Ji, *IEEE Trans. Pattern Anal. Mach. Intell.* **45**, 5782 (2022).
- [68] P. E. Pope, S. Kolouri, M. Rostami, C. E. Martin, and H. Hoffmann, in *IEEE Conf. Comput. Vis. Pattern Recog.* (2019) pp. 10772–10781.
- [69] D. Luo, W. Cheng, D. Xu, W. Yu, B. Zong, H. Chen, and X. Zhang, in *Adv. Neural Inform. Process. Syst.*, Vol. 33 (Curran Associates, Inc., 2020) pp. 19620–19631.
- [70] T. Schnake, O. Eberle, J. Lederer, S. Nakajima, K. T. Schütt, K.-R. Müller, and G. Montavon, *IEEE Trans. Pattern Anal. Mach. Intell.* **44**, 7581 (2022).
- [71] M. Vu and M. T. Thai, in *Adv. Neural Inform. Process. Syst.*, Vol. 33 (Curran Associates, Inc., 2020) pp. 12225–12235.
- [72] R. Ying, D. Bourgeois, J. You, M. Zitnik, and J. Leskovec, GNNExplainer: generating explanations for graph neural networks, in *Adv. Neural Inform. Process. Syst.* (Curran Associates Inc., Red Hook, NY, USA, 2019).
- [73] S. M. Lundberg and S.-I. Lee, *Adv. Neural Inform. Process. Syst.* **30**, 4768–4777 (2017).
- [74] J. H. Friedman, *Ann. Math. Stat.* , 1189 (2001).
- [75] B. Russ, A. Glaudell, J. J. Urban, M. L. Chabiny, and R. A. Segalman, *Nat. Rev. Mater.* **1**, 1 (2016).
- [76] H. Fritzsche, *Solid State Commun.* **9**, 1813 (1971).
- [77] J. Gong, A. Hong, J. Shuai, L. Li, Z. Yan, Z. Ren, and J.-M. Liu, *Phys. Chem. Chem. Phys.* **18**, 16566 (2016).
- [78] J. Qiu, S. Zhi, P. Zhao, J. Wang, X. Ma, S. Ye, C. Lin, X. Zhang, Z. Wu, S. Duan, H. Yao, F. Cao, Q. Zhang, and J. Mao, *Phys. Rev. B* **111**, 045203 (2025).
- [79] C. Molnar, *Interpretable Machine Learning*, 3rd ed. (2025).
- [80] T. L. Meek and L. D. Garner, *J. Chem. Educ.* **82**, 325 (2005).
- [81] D. Adams, *Inorganic Solids*, John Wiley & Sons, London 10.1180/minmag.1975.040.310.19 (1974).
- [82] R.-T. Chen, Z. Hu, and H.-J. Feng, *J. Appl. Phys.* **138**, 023101 (2025).
- [83] G. Sproul, *J. Chem. Educ.* **78**, 387 (2001).
- [84] J. H. Choi, Y. J. Choi, J. W. Lee, W. H. Shin, and J. K. Kang, *Phys. Chem. Chem. Phys.* **11**, 628 (2009).
- [85] M. Yukio, *Intermetallics* **2**, 55 (1994).
- [86] K. Kutorasiński, J. Tobola, and S. Kaprzyk, *Phys. Rev. B* **87**, 195205 (2013).
- [87] R. Rahaman *et al.*, *Adv. Neural Inform. Process. Syst.* **34**, 20063 (2021).
- [88] Y. Zhong, H. Yu, M. Su, X. Gong, and H. Xiang, *npj Comput. Mater.* **9**, 182 (2023).
- [89] Y. Sheng, Y. Wu, J. Yang, W. Lu, P. Villars, and W. Zhang, *npj Comput. Mater.* **6**, 171 (2020).
- [90] H. Kitamura, *Eur. J. Phys.* **36**, 065010 (2015).
- [91] J. B. Smith and H. Ehrenreich, *Phys. Rev. B* **25**, 923 (1982).
- [92] S. Ahmad and S. D. Mahanti, *Phys. Rev. B* **81**, 165203 (2010).

- [93] C. Hu, Z. Gao, M. Zhang, S. Han, C. Fu, and T. Zhu, *Energy Environ. Sci.* **16**, 5381 (2023).
- [94] L. Ward, A. Agrawal, A. Choudhary, and C. Wolverton, *npj Comput. Mater.* **2**, 1 (2016).
- [95] K. Schütt, P.-J. Kindermans, H. E. Saucedo Felix, S. Chmiela, A. Tkatchenko, and K.-R. Müller, in *Adv. Neural Inform. Process. Syst.*, Vol. 30 (Curran Associates, Inc., 2017).
- [96] J. Gastegger, J. Groß, and S. Günnemann, in *Int. Conf. Learn. Represent.* (2020).
- [97] P. Mishra, A. Piktus, G. Goossen, and F. Silvestri, *arXiv preprint arXiv:2001.07524* (2020).
- [98] G. Kresse and J. Furthmüller, *Phys. Rev. B* **54**, 11169 (1996).
- [99] G. Kresse and D. Joubert, *Phys. Rev. B* **59**, 1758 (1999).
- [100] J. P. Perdew, K. Burke, and M. Ernzerhof, *Phys. Rev. Lett.* **77**, 3865 (1996).
- [101] V. Wang, N. Xu, J.-C. Liu, G. Tang, and W.-T. Geng, *Comput. Phys. Commun.* **267**, 108033 (2021).
- [102] G. K. Madsen, J. Carrete, and M. J. Verstraete, *Comput. Phys. Commun.* **231**, 140 (2018).
- [103] Y. Zeng, *TECSA-GNN*.
- [104] Z. Zhang, in *IEEE Int. Symp. Qual. Service* (IEEE, 2018) pp. 1–2.
- [105] A. R. Dunn, *Machine Learning for Semiconducting Solids: Benchmarking, Thermoelectric Discovery, and Dopant Engineering* (University of California, Berkeley, 2023).

**Supplemental Material for**  
*Learning Thermoelectric Transport from Crystal Structures via Multiscale Graph Neural Network*

**Supplementary Note 1. Quantifying the effect of  $E_g$  calculation methods on electronic transport prediction**

In the TECSA-GNN workflow, the band gap  $E_g$  is the only input feature required as prior knowledge. For the training dataset,  $E_g$  is obtained from generalized gradient approximation (GGA) [100] calculations. However, computing  $E_g$  for each candidate during high-throughput screening is impractical. Therefore, we consider employing a pre-trained model to assist in estimating  $E_g$ .

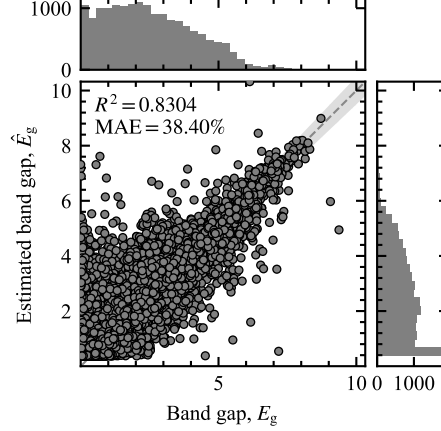


FIG. S1. Parity plot of the predicted  $E_g$ . Here, the  $x$ -axis denotes the DFT-calculated  $E_g$ , while the  $y$ -axis represents the CGCNN-predicted values. The diagonal line serves as the reference, with grey shaded regions indicating the 95% confidence intervals. The histograms along the top and right display the distribution of samples within each range.  $\hat{E}_g$  is the estimated band gap.

The crystal graph convolutional neural network (CGCNN) [20] is a baseline GNN well suited for learning fundamental material properties. In our work, we employ it to predict the band gap  $E_g$  of candidate materials, followed by TECSA-GNN to estimate their electronic transport coefficients. As shown in Fig. S1, the prediction error exhibits a clear distributional dependence, primarily arising from samples with low  $E_g$ . Considering that materials with high PF values are typically semiconductors with relatively low  $E_g$ , we regard  $\hat{E}_g$  as a compromise between efficiency and accuracy for high-throughput screening, rather than a full replacement of DFT in determining the final transport properties of materials.

To further quantify the impact of using  $\hat{E}_g$  on the predictions, Fig. S2 compares the transport property curves obtained from TECSA-GNN when supplied with either  $E_g$  or  $\hat{E}_g$  as input, alongside the results from DFT *ab initio* calculations.

As shown in Fig. S2, the absence of DFT-calculated band gaps as input leads to varying degrees of deviation in the model predictions. For  $\hat{S}_{\hat{E}_g}$ , the discrepancy from the true values remains acceptable, and all three prediction curves converge well as the carrier concentration increases. However, for  $\hat{\sigma}_{\hat{E}_g}$  and  $\hat{\kappa}_{e-\hat{E}_g}$ , the errors at low carrier concentrations reach two to three orders of magnitude, and even at higher concentrations the deviations remain at one to two orders of magnitude. To ensure the reliability of TECSA-GNN predictions, the optimal strategy is to provide DFT-calculated band gaps, followed by the use of a pre-trained band-gap model with higher predictive accuracy.

**Supplementary Note 2. Hyperparameter settings for TECSA-GNN training**

The hyperparameters used to train TECSA-GNN are listed in Tab. S1.

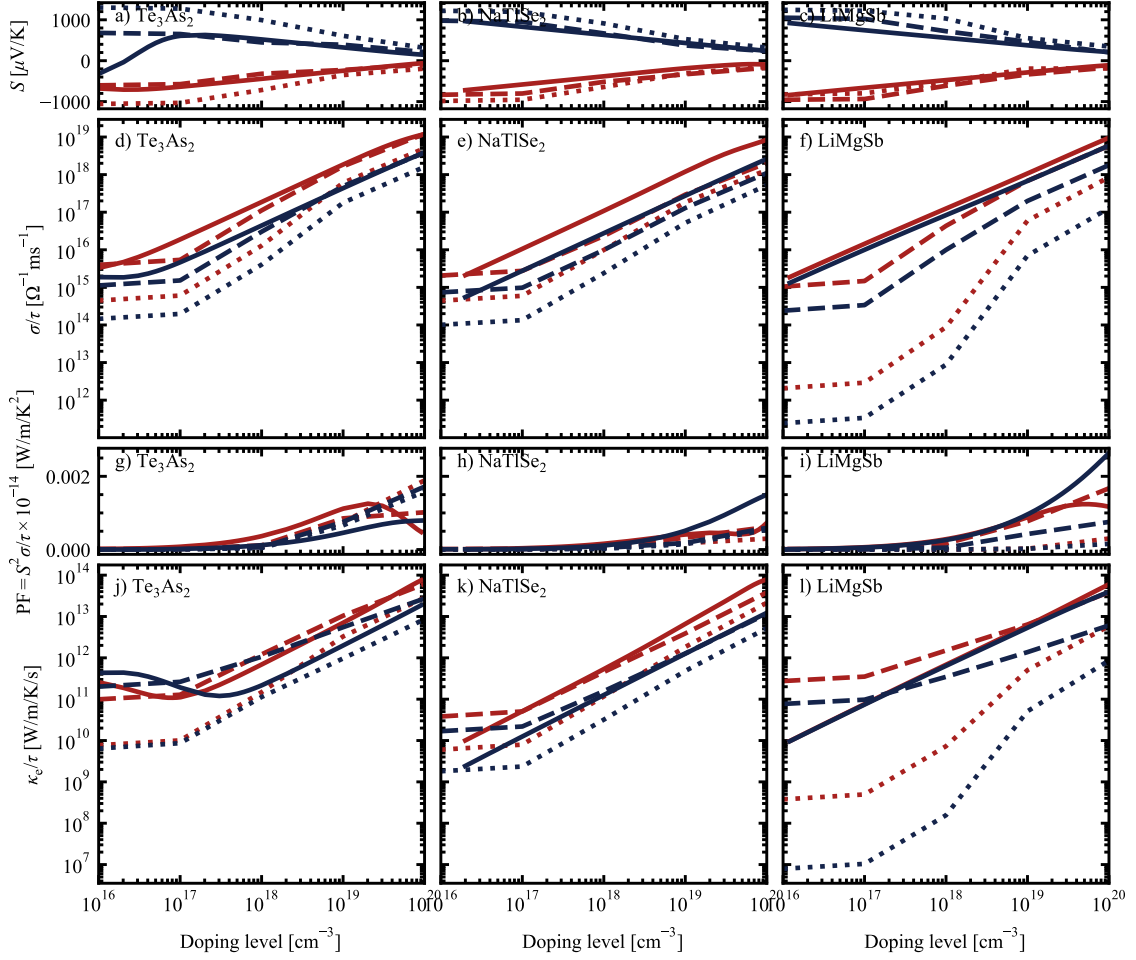


FIG. S2. Doping-concentration-dependent electronic transport coefficients of the candidate materials at 300 K. Here, red denotes  $n$ -type and blue denotes  $p$ -type. Each column corresponds to one compound. Solid, dashed, and dotted lines represent the DFT-calculated values, TECSA-GNN with DFT-calculated  $E_g$ , and TECSA-GNN with CGCNN-predicted  $E_g$ , respectively.

TABLE S1. Hyperparameter settings used for TECSA-GNN training for each target.

Hyperparameter	$S$	$\log(\sigma)$	$\log(\kappa_e)$
Batch size	80	128	128
Initial learning rate	$1 \times 10^{-2}$	$1 \times 10^{-4}$	$1 \times 10^{-4}$
Training epochs	200	2500	2500
Hidden dimension	256	256	256
Number of GConv layers	5	5	5
Optimizer	Adam [104]	Adam [104]	Adam [104]
Weight decay	$1 \times 10^{-5}$	$1 \times 10^{-5}$	$1 \times 10^{-5}$
Loss function	MSE	MSE	MSE

### Supplementary Note 3. Visualizing model embeddings of $\log(\sigma/\tau)$ and $\log(\kappa_e/\tau)$

We extracted the final embedding representations of  $\log(\sigma/\tau)$  and  $\log(\kappa_e/\tau)$  from TECSA-GNN and visualised them in a two-dimensional plane using  $t$ -SNE, as shown in Fig. S3. The visualised samples correspond to  $T = 300$  K and a carrier concentration of  $n = 10^{18}$   $\text{cm}^{-3}$ .

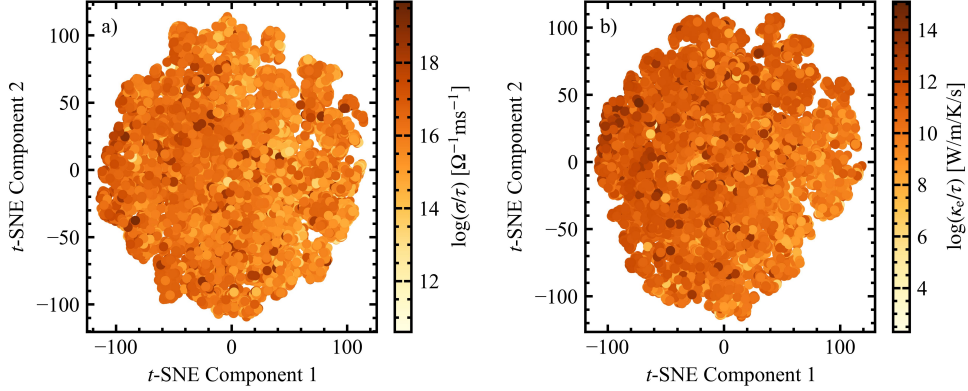


FIG. S3.  $t$ -SNE visualisation. Each point is colour-coded according to its value of (a)  $\log(\sigma/\tau)$  and (b)  $\log(\kappa_e/\tau)$ , respectively.

#### Supplementary Note 4. Global feature importance ranking for $\hat{S}$

In our case, we employ SHAP [73] to quantify the influence of each component of the global feature vector  $\mathbf{U}$  on the model’s predictions. Within  $\mathbf{U}$ , the band gap  $E_g$  is supplied as prior knowledge, whereas all remaining dimensions are automatically constructed from the Magpie descriptors [94] based solely on the chemical formula. Magpie features are widely used in TE property prediction [10, 31, 105]; each carries a clear physical meaning, yet they are rather elementary and therefore not immediately suitable for elucidating the connection between fundamental material properties and electronic transport performance.

TABLE S2. Global feature importance ranked by mean absolute SHAP value.

Rank	Global feature	Mean-absolute SHAP value
1	gap ( $E_g$ )	0.014344
2	MagpieData range Electronegativity ( $\Delta\chi$ )	0.012311
3	frac p valence electrons ( $f_p$ )	0.012232
4	MagpieData range MendeleevNumber	0.009984
5	MagpieData avg_dev Row	0.008366
6	MagpieData mean SpaceGroupNumber	0.008150
7	3-norm	0.007775
8	MagpieData minimum MendeleevNumber	0.007489
9	MagpieData mean MendeleevNumber	0.007297
10	MagpieData minimum Column	0.007127
11	MagpieData minimum Electronegativity	0.007092
12	MagpieData range SpaceGroupNumber	0.007067
13	MagpieData maximum NdValence	0.006795
14	MagpieData mode Row	0.006782
15	MagpieData range Column	0.006457
16	MagpieData avg_dev NsUnfilled	0.005798
17	MagpieData minimum NpValence	0.005114
18	MagpieData avg_dev NfValence	0.004988
19	MagpieData range MeltingT	0.004982
20	MagpieData mean GSvolume_pa	0.004847

In the main text, we provide physical interpretations for three representative features, namely the band gap ( $E_g$ ), the MagpieData range of electronegativity ( $\Delta\chi$ ), and the fraction of  $p$ -valence electrons ( $f_p$ ). For reference, we list here the top twenty features ranked by their mean-absolute SHAP values (see Tab. S2), while a more comprehensive table is available online [103].

### Supplementary Note 5. Ablation studies and model efficiency assessment

The necessity of the model design and the appropriateness of the hyperparameter settings must be cross-validated through ablation studies. Here, we discuss the effects of varying the number of graph convolution layers, as well as the presence or absence of the global features  $\mathbf{U}$  and the attention weights  $\tilde{\alpha}_{ij}$  in the graph convolution process (see Eq. (5)), on both model performance and computational efficiency.

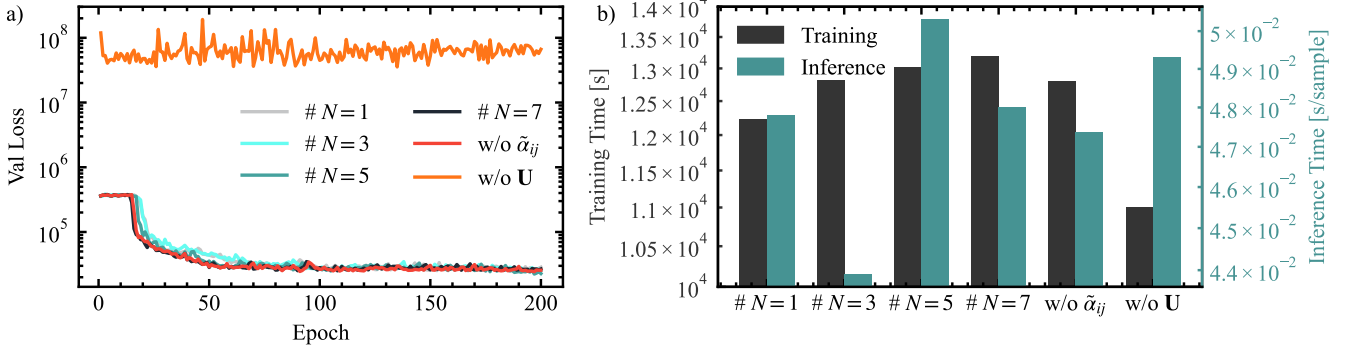


FIG. S4. Ablation study results. (a) Test-set MSE loss curves under different configurations; all models were trained for 200 epochs. (b) Model efficiency evaluated in terms of training time (left  $y$ -axis) and inference time per sample (right  $y$ -axis).

For simplicity, we set the learning task to  $p$ -type  $S$  at  $T = 300$  K and  $n = 10^{20}$   $\text{cm}^{-3}$ , using only 1,024 samples for the ablation study. In Fig. S4,  $\# N = 5$  corresponds to the standard model used in the main text. In Fig. S4(a), it is evident that removing  $\mathbf{U}$  leads to a substantial drop in performance, indicating that  $\mathbf{U}$  is indispensable for learning  $S$ . By contrast, within the limited number of training epochs, the standard model achieves near-optimal extrapolation, though differences with other configurations are minor. As shown in Fig. S4(b), training time increases significantly with model complexity, whereas higher complexity does not guarantee superior accuracy. For example, the  $\# N = 7$  configuration requires the longest training time but achieves slightly lower accuracy than the standard setting. Interestingly, inference time per sample does not show a clear positive correlation with model complexity, though overall differences are small, possibly due to stochastic effects. Additionally, computing the attention weights increases training time by only  $\sim 1.7\%$  while noticeably improving model performance. The performance of TECSA-GNN without  $\mathbf{U}$  is shown in Fig. S5.

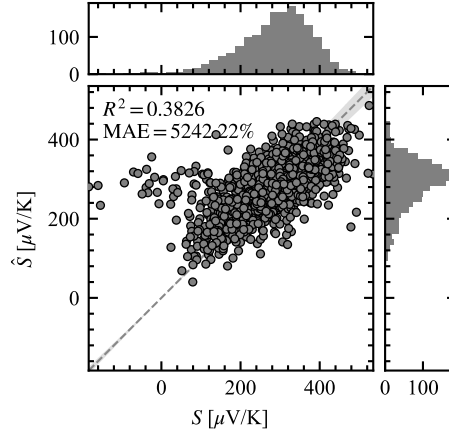


FIG. S5. Parity plot of the TECSA-GNN (w/o  $\mathbf{U}$ ) predicted  $S$ .

The computations were conducted on a single node equipped with dual Intel Xeon E5-2640v4 Broadwell processors (2.4 GHz, 20 cores in total) and 128 GB of ECC DDR4 memory running at 2400 MHz. The node was fitted with four NVIDIA Tesla V100 Volta GPUs, each with 16 GB of memory and connected via NVLink. Nodes were interconnected using Intel Omni-Path Architecture (OPA) at 100 Gbps. Jobs were submitted via SLURM using one node, four tasks

per node, and one GPU per task (#SBATCH -nodes=1, #SBATCH -ntasks-per-node=4, #SBATCH -gres=gpu:1).

### Supplementary Note 6. Complete set of candidate materials in high-throughput screening

Tab. S3 lists the complete set of Materials Project compounds that satisfy the screening criteria described in the main text, together with their estimated maximum PF values. Here, the PF is computed from the TECSA-GNN predictions of  $S$  and  $\log(\sigma/\tau)$ . It should be noted that the training data for TECSA-GNN include only five discrete doping levels,  $n = \{10^{16}, 10^{17}, \dots, 10^{20}\} \text{ cm}^{-3}$ , whereas interpolation over  $n$  is performed at prediction time to identify the potential maximum PF.

TABLE S3. TECSA-GNN estimations of transport coefficients for unlabeled compounds. Shown here are the maximum PF values at 300 K for different Types, together with their corresponding optimal carrier concentrations.

Formula	MPID	$E_g$ [eV]	$\hat{S}$ [ $\mu\text{V}/\text{K}$ ]	$\log(\hat{\sigma}/\tau)$ [ $\Omega^{-1}\text{ms}^{-1}$ ]	PF [ $\text{W}/\text{m}/\text{K}^2$ ]	$\log(\hat{\kappa}_e/\tau)$ [ $\text{W}/\text{m}/\text{K}/\text{s}$ ]	$n$ [ $\text{cm}^{-3}$ ]	Type
AgBr	mp-23231	0.892566	-144.483	18.6356	$9.02083 \times 10^{-4}$	13.0869	$7.74264 \times 10^{18}$	$n$
AgBr	mp-23231	0.892566	262.102	19.2244	$1.15167 \times 10^{-2}$	13.7538	$1 \times 10^{20}$	$p$
Ba <sub>2</sub> BiAu	mp-862947	0.594404	-61.1141	18.5928	$1.46252 \times 10^{-4}$	13.796	$1 \times 10^{20}$	$n$
Ba <sub>2</sub> BiAu	mp-862947	0.594404	139.252	18.8547	$1.38761 \times 10^{-3}$	13.8048	$1 \times 10^{20}$	$p$
Be <sub>2</sub> C	mp-1569	3.25563	-81.1867	18.5755	$2.48017 \times 10^{-4}$	13.6666	$1 \times 10^{20}$	$n$
Be <sub>2</sub> C	mp-1569	3.25563	301.828	18.1609	$1.31955 \times 10^{-3}$	13.0739	$1 \times 10^{20}$	$p$
Ca <sub>2</sub> SnHg	mp-866229	0.371006	-159.031	18.3182	$5.26192 \times 10^{-4}$	13.1323	$1.6681 \times 10^{19}$	$n$
Ca <sub>2</sub> SnHg	mp-866229	0.371006	117.316	19.0473	$1.53463 \times 10^{-3}$	13.907	$1 \times 10^{20}$	$p$
Ca <sub>3</sub> SbN	mp-1013548	0.425918	-76.5836	18.6506	$2.62320 \times 10^{-4}$	13.6365	$1 \times 10^{20}$	$n$
Ca <sub>3</sub> SbN	mp-1013548	0.425918	234.786	18.4904	$1.70513 \times 10^{-3}$	13.3353	$1 \times 10^{20}$	$p$
Ca <sub>3</sub> SbP	mp-1013550	0.723543	-327.009	17.7392	$5.86506 \times 10^{-4}$	12.724	$7.74264 \times 10^{18}$	$n$
Ca <sub>3</sub> SbP	mp-1013550	0.723543	431.911	17.8878	$1.44090 \times 10^{-3}$	12.5791	$1 \times 10^{19}$	$p$
CaTe	mp-1519	2.2022	-305.570	18.2146	$1.53050 \times 10^{-3}$	13.0434	$1.6681 \times 10^{19}$	$n$
CaTe	mp-1519	2.2022	197.779	18.6527	$1.75812 \times 10^{-3}$	13.5042	$1 \times 10^{20}$	$p$
Cs <sub>2</sub> Se	mp-1011695	1.72709	-142.612	18.2735	$3.81776 \times 10^{-4}$	12.7727	$1 \times 10^{19}$	$n$
Cs <sub>2</sub> Se	mp-1011695	1.72709	497.458	18.0665	$2.88444 \times 10^{-3}$	12.1803	$1 \times 10^{20}$	$p$
CsAu	mp-2667	0.872012	-229.414	17.9560	$4.75549 \times 10^{-4}$	12.5922	$1 \times 10^{19}$	$n$
CsAu	mp-2667	0.872012	204.624	18.1583	$6.02830 \times 10^{-4}$	12.8400	$1.6681 \times 10^{19}$	$p$
CsSnI <sub>3</sub>	mp-614013	0.796505	-105.031	18.6524	$4.95455 \times 10^{-4}$	13.3473	$1 \times 10^{20}$	$n$
CsSnI <sub>3</sub>	mp-614013	0.796505	181.039	18.3133	$6.74244 \times 10^{-4}$	12.7785	$1 \times 10^{20}$	$p$
LiBeSb	mp-1100398	0.717294	-162.014	18.6789	$1.25323 \times 10^{-3}$	12.9513	$1 \times 10^{20}$	$n$
LiBeSb	mp-1100398	0.717294	174.554	18.5885	$1.18128 \times 10^{-3}$	13.3151	$1 \times 10^{20}$	$p$
Mg <sub>3</sub> SbN	mp-1080847	0.411554	-184.658	18.0349	$3.69528 \times 10^{-4}$	12.9398	$1.29155 \times 10^{19}$	$n$
Mg <sub>3</sub> SbN	mp-1080847	0.411554	268.594	18.2413	$1.25757 \times 10^{-3}$	13.1031	$1 \times 10^{20}$	$p$
Na <sub>3</sub> BrO	mp-985586	2.04698	-178.518	17.6186	$1.32432 \times 10^{-4}$	12.3056	$7.74264 \times 10^{18}$	$n$
Na <sub>3</sub> BrO	mp-985586	2.04698	443.979	18.1098	$2.53829 \times 10^{-3}$	12.5663	$1 \times 10^{20}$	$p$
NaCaAs	mp-961685	1.44325	-161.470	18.7646	$1.51631 \times 10^{-3}$	13.2748	$5.99484 \times 10^{19}$	$n$
NaCaAs	mp-961685	1.44325	235.497	18.6640	$2.55830 \times 10^{-3}$	12.8157	$1 \times 10^{20}$	$p$
NbAlFe <sub>2</sub>	mp-865280	0.370744	-335.134	16.8515	$7.97843 \times 10^{21}$	12.7587	$3.59381 \times 10^{19}$	$n$
NbAlFe <sub>2</sub>	mp-865280	0.370744	182.024	16.9432	$2.90697 \times 10^{21}$	12.8261	$3.59381 \times 10^{19}$	$p$
ScTeRh	mp-1100405	0.371298	-225.648	18.5407	$1.76824 \times 10^{-3}$	12.9381	$1 \times 10^{20}$	$n$
ScTeRh	mp-1100405	0.371298	174.631	18.8094	$1.96622 \times 10^{-3}$	12.9849	$1 \times 10^{20}$	$p$
Sr <sub>2</sub> BiAu	mp-867193	0.887706	-293.429	17.3135	$1.77227 \times 10^{-4}$	12.7495	$5.99484 \times 10^{18}$	$n$
Sr <sub>2</sub> BiAu	mp-867193	0.887706	186.861	18.2078	$5.63403 \times 10^{-4}$	13.3359	$7.74264 \times 10^{19}$	$p$
Sr <sub>2</sub> HgPb	mp-867207	0.3883	-50.5417	19.4284	$6.85017 \times 10^{-4}$	13.9563	$1 \times 10^{20}$	$n$
Sr <sub>2</sub> HgPb	mp-867207	0.3883	140.726	19.1157	$2.58481 \times 10^{-3}$	13.8960	$7.74264 \times 10^{19}$	$p$
Sr <sub>2</sub> SnHg	mp-867169	0.399424	-53.1025	19.1148	$3.67271 \times 10^{-4}$	13.8076	$1 \times 10^{20}$	$n$
Sr <sub>2</sub> SnHg	mp-867169	0.399424	113.689	19.1426	$1.79507 \times 10^{-3}$	13.8929	$1 \times 10^{20}$	$p$
Sr <sub>3</sub> AsN	mp-1013555	0.395546	-88.6047	18.4016	$1.97951 \times 10^{-4}$	13.3923	$1.6681 \times 10^{19}$	$n$
Sr <sub>3</sub> AsN	mp-1013555	0.395546	207.370	19.0305	$4.61272 \times 10^{-3}$	13.6461	$1 \times 10^{20}$	$p$
Sr <sub>3</sub> PN	mp-1013554	1.28907	-94.2097	18.3728	$2.09399 \times 10^{-4}$	13.8673	$4.64159 \times 10^{19}$	$n$
Sr <sub>3</sub> PN	mp-1013554	1.28907	278.465	18.2381	$1.34181 \times 10^{-3}$	13.0319	$1 \times 10^{20}$	$p$
TiFeTe	mp-961673	0.37538	-142.810	17.9597	$1.85885 \times 10^{-4}$	13.2200	$2.78256 \times 10^{19}$	$n$
TiFeTe	mp-961673	0.37538	173.601	18.7217	$1.58777 \times 10^{-3}$	13.1356	$1 \times 10^{20}$	$p$
TiSnPd	mp-961682	0.387674	-147.091	17.8063	$1.38512 \times 10^{-4}$	13.3154	$1 \times 10^{20}$	$n$

Continued on next page

TABLE S3 – continued from previous page

Formula	MPID	$E_g$ [eV]	$\hat{S}$ [ $\mu\text{V}/\text{K}$ ]	$\log(\hat{\sigma}/\tau)$ [ $\Omega^{-1}\text{ms}^{-1}$ ]	PF [ $\text{W}/\text{m}/\text{K}^2$ ]	$\log(\hat{\kappa}_e/\tau)$ [ $\text{W}/\text{m}/\text{K}/\text{s}$ ]	$n$ [ $\text{cm}^{-3}$ ]	Type
TiSnPd	mp-961682	0.387674	383.367	17.8564	$1.05592 \times 10^{-3}$	13.4627	$1 \times 10^{20}$	<i>p</i>
ZrAsIr	mp-1093991	0.392472	-238.796	18.5689	$2.11344 \times 10^{-3}$	14.3142	$5.99484 \times 10^{19}$	<i>n</i>
ZrAsIr	mp-1093991	0.392472	90.8224	19.0388	$9.01872 \times 10^{-4}$	14.5636	$1 \times 10^{20}$	<i>p</i>
ZrInAu	mp-961693	0.372816	-301.837	17.9959	$9.02412 \times 10^{-4}$	13.2829	$2.15443 \times 10^{19}$	<i>n</i>
ZrInAu	mp-961693	0.372816	386.194	17.9940	$1.47087 \times 10^{-3}$	13.1987	$1.6681 \times 10^{19}$	<i>p</i>
ZrSnPd	mp-961687	0.393361	-311.060	17.9411	$8.44845 \times 10^{-4}$	13.5349	$7.74264 \times 10^{19}$	<i>n</i>
ZrSnPd	mp-961687	0.393361	238.129	17.8324	$3.85460 \times 10^{-4}$	13.3979	$7.74264 \times 10^{19}$	<i>p</i>
ZrSnPt	mp-961713	0.371496	-214.953	18.3646	$1.06973 \times 10^{-3}$	13.7095	$7.74264 \times 10^{19}$	<i>n</i>
ZrSnPt	mp-961713	0.371496	174.251	18.4250	$8.07878 \times 10^{-4}$	13.7230	$7.74264 \times 10^{19}$	<i>p</i>